

Through-the-Wall Radar Human Activity Micro-Doppler Signature Representation Method Based on Joint Boulic-Sinusoidal Pendulum Model

Xiaopeng Yang[✉], Senior Member, IEEE, Weicheng Gao[✉], Graduate Student Member, IEEE, Xiaodong Qu[✉], Member, IEEE, Zeyu Ma[✉], Student Member, IEEE and Hao Zhang[✉], Student Member, IEEE

Abstract—With the help of micro-Doppler signature, ultra-wideband (UWB) through-the-wall radar (TWR) enables the reconstruction of range and velocity information of limb nodes to accurately identify indoor human activities. However, existing methods are usually trained and validated directly using range-time maps (RTM) and Doppler-time maps (DTM), which have high feature redundancy and poor generalization ability. In order to solve this problem, this paper proposes a human activity micro-Doppler signature representation method based on joint Boulic-sinusoidal pendulum motion model. In detail, this paper presents a simplified joint Boulic-sinusoidal pendulum human motion model by taking head, torso, both hands and feet into consideration improved from Boulic-Thalmann kinematic model. The paper also calculates the minimum number of key points needed to describe the Doppler and micro-Doppler information sufficiently. Both numerical simulations and experiments are conducted to verify the effectiveness. The results demonstrate that the proposed number of key points of micro-Doppler signature can precisely represent the indoor human limb node motion characteristics, and substantially improve the generalization capability of the existing methods for different testers.

Index Terms—through-the-wall radar, human activity recognition, micro-Doppler signature, feature extraction, corner representation.

I. INTRODUCTION

INDOOR human activity recognition has gradually become a popular research topic in the field of radar and intelligent signal interpretation [1]–[6]. In the literature, contact devices, cameras, mmWave radar, and WIFI were devoted for activity recognition [2], [7]. Recently, UWB TWR was also employed, which could penetrate the wall and work under complex environments, avoiding privacy and security issues, and has been used in different applications [8]–[16].

Manuscript received January 15th, 2024; revised XXXXXXXX XXth, 2024; accepted XXXXXXXX XXth, 2024. Date of publication XXXXXXXX XXth, 2024; date of current version XXXXXXXX XXth, 2024. This work was supported in part by the National Natural Science Foundation of China under Grant 62101042. This work was also supported in part by Beijing Institute of Technology Research Fund Program for Young Scholars under Grant XSQD-202205005. (Corresponding author: Xiaodong Qu.)

Xiaopeng Yang, Zeyu Ma, and Hao Zhang, are with the School of Information and Electronics, Beijing Institute of Technology, Beijing 100081, China, and also with the Jiaxing Research Center of Beijing Institute of Technology, Jiaxing 314000, China (email: xiaopengyang@bit.edu.cn; 3220220653@bit.edu.cn; 3220220662@bit.edu.cn).

Weicheng Gao, and Xiaodong Qu, are with the School of Information and Electronics, Beijing Institute of Technology, Beijing 100081, China, and with the Key Laboratory of Electronic and Information Technology in Satellite Navigation, Beijing Institute of Technology, Beijing 100081, China (e-mail: JoeyBG@126.com; xdqu@bit.edu.cn).

Digital Object Identifier 10.1109/TMTT.2024.XXXXXXX

Over the past decade, researchers have made many contributions in the area of signal processing for radar-based indoor human monitoring. HAR required spatial motion information over a period of time, and the recognition of different activities required complex micro-Doppler signature decoding process [17]. Zhang *et al.* employed Doppler radar and extracted micro-Doppler signature based on the difference of micro-motions between the warhead and decoys for human gait imaging [18]. Gao *et al.* also improved and verified these theories by simulations [19]. Smith *et al.* used dynamic time warping to study radar micro-Doppler signature [20], and highlighted the difficulties for classification. Fioranelli *et al.* presented human micro-Doppler signature data gathered by a multi-static radar system to discriminate unarmed and potentially armed personnel walking along different trajectories [21]. A feature extraction method based on micro-Doppler signature was proposed by Du *et al.* to categorize ground moving targets into three kinds, i.e., single walking person, double people walking, and a moving wheeled vehicle [22]. Chen *et al.* introduced a series of statistical techniques for automatic hand, arm or body gesture recognition [23], and some other influential works for improvement [24], [25]. Although these methods considered the principle of micro-Doppler signature, their extraction process was achieved by parametric estimation or image transformation, resulted in lower accuracy.

With the rapid development of AI, many deep-learning-based methods have been proposed for HAR. For example, Li *et al.* elaborated neural network for HAR using 1D, 2D, and 3D radar echoes [26]. Singh *et al.* proposed a framework for accurate HAR based on sparse and non-uniform point clouds [27]. Cheng *et al.* proposed a novel range profile sequence driven end-to-end method, which employed random cropping training for better model performance [28]. Ahmad *et al.* proposed AEN to achieve refined micro-Doppler signature extraction at low noise levels [29]. Jia *et al.* proposed a radar image classification scheme using ResNet [30], which aimed to achieve higher network depth and better recognition accuracy. In order to learn the long range timing information, Yang *et al.* proposed an LSTM-based classifier [31] to train and inference the sliced radar images. Guo *et al.* proposed to use PGM [32] to achieve radar image feature extraction with certain topological modeling capabilities. Furthermore, a variety of methods based on feature representation learning were investigated [33], achieving finer-grained micro-Doppler signature extraction [34] or faster inference speeds [35], respectively. These methods, although solving the problem of

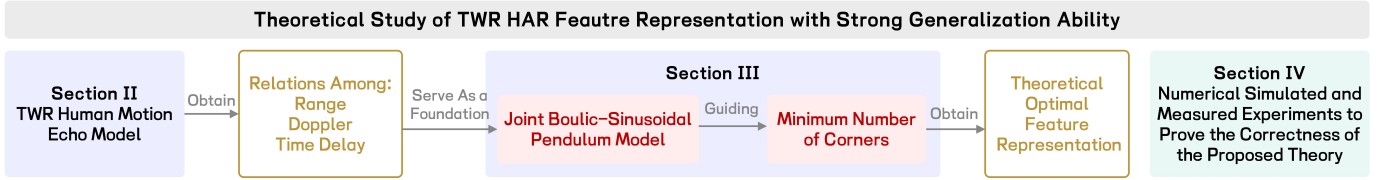


Fig. 1. The logic of the construction of the proposed theoretical work and the structure of the paper.

low accuracy, were often implemented by directly iterating the pseudo-RGB mapping of the radar RTM or DTM, which meant that the interpretability of the micro-Doppler signature extraction was poor [36]. In addition, neural networks needed to be trained on large data sets, but the radar data acquisition of human activity were difficult and limited in number (In the vast majority of instances, the amount of data was much smaller than the number of parameters in the network), which meant that the final trained model was very prone to overfitting [37]. As a result, it was difficult for these methods to have good generalization capability to different testers.

Relevant results demonstrated that the generalization performance of machine learning could be effectively improved through data processing, feature selection, regularization, cross-validation, or model tuning [38], [39]. Constrained by the data and resource requirements of radar systems, feature selection and dimension reduction are the best choices to improve the generalization capability. Therefore, it is necessary to propose a micro-Doppler signature representation method based on mathematical-physical background that has a much smaller number of parameters but effectively characterizes the complete micro-Doppler information [40].

In this paper, **TWR human activity feature can be represented by 30 key points for both range and Doppler profiles, which can effectively represent the complete micro-Doppler information while maximizing the generalization capability of indoor HAR across different testers.** The key points reflect the inflection points, stationary points, curve intersections, and intersections of the curves with the axes for each limb node on both range profiles and the Doppler profiles. These key points are defined in the rest of this paper as “Micro-Doppler Corner Feature”. Based on the works of Boulic and Thalmann [41], in this paper, a kinematic model dedicated for feature dimension reduction analysis is presented, and the minimum number of corner points required to be able to represent the complete micro-Doppler information of various types of indoor human activities is calculated. Moreover, simulation and real-world experiments are conducted to demonstrate the effectiveness, efficiency, and generalization capability of the proposed micro-Doppler corner representation.

As shown in Fig. 1, the rest of the paper is organized as follows: Section II introduces the TWR signal model, followed by Section III, which introduces the proposed human motion model, and discusses the minimum number of corners. Section IV gives numerical simulated and measured experimental verification. Section V gives the conclusion. Details of a feasible feature extractor can be found in the Appendix.

II. TWR-BASED HUMAN MOTION ECHO MODEL

Human target is approximately equivalent to a superposition of different limb nodes as scattering centers. The distance and relative velocity of each node are reflected as the time delay and Doppler information in the echo [42]. Assuming the radar emits LFMCW signal. One CPI contains M PRI. Then the time domain signal in the m^{th} PRI can be expressed as:

$$S_{\text{tx},m}(t) = A_{\text{tx}} e^{j(2\pi(f_c(t-mT_s) + \frac{1}{2}\mu(t-mT_s)^2) + \varphi_{\text{tx}})} \quad , \quad mT_s \leq t \leq (m+1)T_s \quad (1)$$

where A_{tx} is the amplitude. T_s is the PRI. $\mu = \frac{B}{T_s}$ is the chirp rate, B is the bandwidth. f_c is the carrier frequency. φ_{tx} is the initial phase.

Assume that the N_i node of the body currently under consideration has a reflectivity of η_{N_i} . Introduce a two-way time delay $\tau_{N_i}(t) = \frac{2\xi_{N_i}}{c}$, where c is the speed of light. Then, the time-domain echo signal of the radar can be expressed as:

$$S_{\text{rx},N_i,m}(t) = A_{\text{rx},N_i} e^{j(2\pi(f_c t_{N_i} + \frac{1}{2}\mu t_{N_i}^2) + \varphi_{\text{rx}})} \quad (2)$$

$$t_{N_i} = t - mT_s - \tau_{N_i}(t), \quad mT_s \leq t \leq (m+1)T_s$$

where $A_{\text{rx},N_i} = \eta_{N_i} A_{\text{tx}}$, $\varphi_{\text{rx}} = \varphi_{\text{tx}}$. After mixing the echo with the transmitted signal, the following can be obtained:

$$S_{\text{mix},N_i,m}(t) = S_{\text{tx},m}(t) \cdot S_{\text{rx},N_i,m}(t) \quad (3)$$

$$= A_{\text{tx}} A_{\text{rx},N_i} e^{j f_{\text{mix},N_i}(t)},$$

where,

$$f_{\text{mix},N_i}(t) = 2\pi f_c(t - mT_s) + \pi\mu(t - mT_s)^2 \quad (4)$$

$$+ \varphi_{\text{tx}} + \varphi_{\text{rx}} + 2\pi f_c(t - mT_s - \tau_{N_i}(t))$$

$$+ \pi\mu(t - mT_s - \tau_{N_i}(t))^2$$

$$= 4\pi f_c(t - mT_s) - 2\pi f_c \tau_{N_i}(t)$$

$$+ 2\pi\mu(t - mT_s)^2 + 2\varphi_{\text{tx}}$$

$$- 2\pi\mu(t - mT_s)\tau_{N_i}(t) + \pi\mu\tau_{N_i}^2(t)$$

$$mT_s \leq t \leq (m+1)T_s$$

Thus, after low-pass filtering, the base-band echo of the N_i node of the human target is obtained:

$$S_{b,N_i,m}(t) = \frac{1}{2} A_{\text{rx},N_i} A_{\text{tx}} e^{j f_{\text{mix},re,N_i}(t)} \quad (5)$$

$$= A_{b,N_i} e^{j2\pi(f_c \tau_{N_i}(t) - \frac{1}{2}\mu\tau_{N_i}^2(t) + \mu(t-mT_s)\tau_{N_i}(t))}$$

$$= A_{b,N_i} e^{j2\pi(f_c \tau_{N_i}(t) - \frac{1}{2}\mu\tau_{N_i}^2(t) + \mu(t-mT_s)\tau_{N_i}(t))}$$

$$A_{b,N_i} = \frac{1}{2} \eta_{N_i} A_{\text{tx}}^2, \quad mT \leq t \leq (m+1)T$$

Summing radar echoes for different human limb nodes defined in TABLE I, the complete time domain base-band

TABLE I
CONSTRAINTS OF THE PROPOSED HUMAN MOTION MODEL*.

Name of Nodes	Initial Position (m)	Initial Velocity (m/s)
Head (N_1)	$(x_1, y_1, h_1 + 0.15)$	$(v_{1x}, v_{1y}, 0)$
Torso (N_2)	$(x_1, y_1, \frac{h_1+h_2}{2})$	$(v_{1x}, v_{1y}, 0)$
Name of Nodes	Constraints ¹	
Hands (N_3 & N_4)	$\ \text{Hand} - \text{Torso}_1 \ = l_1$	
Feet (N_5 & N_6)	$\ \text{Foot} - \text{Torso}_2 \ = l_2$	

* The six points are determined by a combination of the key information in human motion, as well as the TWR wavelength with range resolution.

¹ **Hand**, **Foot**, **Torso₁**, and **Torso₂** denote the coordinates of hand nodes, foot nodes, upper torso node, and lower torso node, respectively.

TABLE II
EXAMPLES OF HUMAN LIMB NODES' MOTION*.

Serial Number	Motion States	Nodes Included
Natural Walking¹		
(1)	Acceleration-Free Motion	N_1, N_2
(2)	Sinusoidal Pendulum	N_3, N_4, N_5, N_6
(3)	Sudden Acceleration	/
In-situ Acceleration²		
(1)	Acceleration-Free Motion	/
(2)	Sinusoidal Pendulum	/
(3)	Sudden Acceleration	$N_1, N_2, N_3, N_4, N_5, N_6$
Combinations³		
(1)	Acceleration-Free Motion	N_1, N_2
(2)	Sinusoidal Pendulum	N_3, N_4, N_5, N_6
(3)	Sudden Acceleration	$N_1, N_2, N_3, N_4, N_5, N_6$

* Two typical activities are considered. Other indoor human activities can be corresponded to each motion states in turn. "/" denotes that none of the nodes is associated with the current motion state. Definitions of limb nodes $N_1 \sim N_6$ are consistent in TABLE I.

¹ Activities that can be approximated to be classified as natural walking include walking, kicking, punching, and rotation. The design idea is that the motion state of each limb node in these activities can be seen in a state of periodic oscillation.

² Activities that can be approximated to be classified as in-situ acceleration include grabbing, standing up, and sitting down. The design idea is that the motion state of each limb node in these activities can be seen as a falling process of first acceleration and then deceleration.

³ Activities that can be approximated to be classified as the combinations include walking to sitting, sitting to walking, walking to falling, and falling to walking. The design idea is that the limb nodes of the human body swing periodically around a certain center, and at the same time there are acceleration and deceleration processes in that center.

radar echo is obtained:

$$\begin{aligned}
 S_{b,m}(t) &= \sum_{i=1}^6 S_{b,N_i,m}(t) + S_{b,\text{Wall},m} + S_{b,\text{Noise},m} \\
 &= \sum_{i=1}^6 A_{b,N_i} e^{j2\pi(f_c \tau_{N_i}(t) - \frac{1}{2} \mu \tau_{N_i}^2(t) + \mu(t - mT_s) \tau_{N_i}(t))} \\
 &\quad + S_{b,\text{Wall},m} + S_{b,\text{Noise},m}
 \end{aligned} \tag{6}$$

where $S_{b,\text{Wall},m}$ is the echo component of the wall, and $S_{b,\text{Noise},m}$ is the noise component.

III. OPTIMAL CORNER REPRESENTATION OF MICRO-DOPPLER SIGNATURE

In this section, we first develop the joint Boulic-sinusoidal pendulum model. Then, we discuss the minimum required

number of corners to maximize feature dimension reduction while preserving human motion information.

A. Joint Boulic-Sinusoidal Pendulum Model

As shown in Fig. 2, the proposed joint Boulic-sinusoidal pendulum model consists of two stages. The first is human structure model, which is the simplified version of the Boulic-Thalmann limb-node model [41]. The second is gait pattern model, which utilizes an approximation of the pendulum model with a sinusoidal period [43]. Considering the range and Doppler resolution of UWB radars [8], human structure model contains only seven nodes can effectively characterize the motion information: the head, the upper edge of the torso, the lower edge of the torso, both hands, and both feet. Note that the torso is designed as an individual node using the center-of-scattering method [44]. Therefore, the human model proposed in this paper only contains six limb nodes in total.

Assume that the radar observation location is fixed at $(0, 0, h_0)$, the initial position of the human body is $(x_1, y_1, 0)$, the arm length is l_1 , and the leg length is l_2 . The heights of the upper and lower edges of the torso from the ground are h_1 and h_2 , respectively. The initial speed of the body is $(v_{1x}, v_{1y}, \alpha\varphi)$, where α is the magnitude of human micro-undulation motion in Z-direction, φ is the gait frequency. The resulting motion constraints for the six nodes are shown in TABLE I. For common human indoor activities [1], the micro-Doppler signature can be regarded as: (1) Natural Walking, (2) In-situ Acceleration, or (3) Their combinations shown in TABLE II. Therefore, in the following, the mathematical models of range and velocity curves for different nodes under (1) and (2) are derived, respectively.

1. Natural Walking

1.1. Head Node N_1

At moment t , the distance between the head node N_1 and radar is:

$$\begin{aligned}
 R_{\text{He}} &= (R_1'^2 + 2(x_1 v_{1x} + y_1 v_{1y})t + v_1^2 t^2 \\
 &\quad - h_1^2 + (h_1 - h_0 + \omega(t) + 0.15)^2)^{\frac{1}{2}},
 \end{aligned} \tag{7}$$

where:

$$R_1' = \sqrt{x_1^2 + y_1^2 + h_1^2}, \quad v_1 = \sqrt{v_{1x}^2 + v_{1y}^2}, \tag{8}$$

and:

$$\omega(t) = \alpha \sin(\varphi t), \tag{9}$$

is the micro-undulation process during human motion, $h_1 - h_0 + 0.15 \gg \alpha$. The effect on velocity is then superimposed component in the z-axis that:

$$\omega'(t) = \alpha \varphi \cos(\varphi t). \tag{10}$$

The distance R_{He} can be rewritten as:

$$R_{\text{He}} \approx (R_1^2 + 2(x_1 v_{1x} + y_1 v_{1y})t + v_1^2 t^2)^{\frac{1}{2}}, \tag{11}$$

where:

$$R_1 = \sqrt{x_1^2 + y_1^2 + (h_1 - h_0 + 0.15)^2}. \tag{12}$$

In practice, $R_{\text{He,real}} = R_{\text{He}}$ for free space, and:

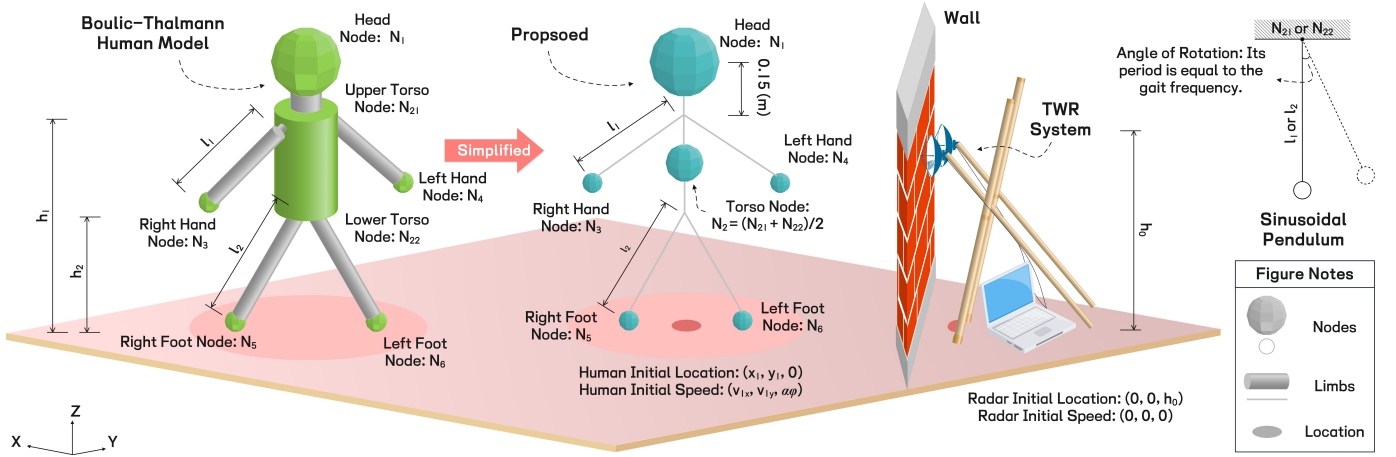


Fig. 2. Schematic diagram of the proposed joint Boulic-sinusoidal pendulum model.

$$R_{\text{He,real,TWR}} \approx R_{\text{He}} + d(\sqrt{\epsilon_r} - 1), \quad (13)$$

for through-the-wall detection, where d, ϵ_r are the thickness and relative permittivity of the wall, respectively.

Define one-way propagation distance as ξ_{N_1} . Then,

$$\xi_{N_1}^2 = v_1^2 t^2 + 2(x_1 v_{1x} + y_1 v_{1y})t + R_1^2, \quad (14)$$

which is a quadratic function with respect to t . Thus, we only need three different points to uniquely determine the analytic form of the function. In general, the two points intersecting the front and back edges of the observed time window and the extreme points are used:

(1) When $t = 0$, we get:

$$\xi_{N_1}^2 = R_1^2. \quad (15)$$

(2) When $t = T$, we get:

$$\xi_{N_1}^2 = v_1^2 T^2 + 2(x_1 v_{1x} + y_1 v_{1y})T + R_1^2, \quad (16)$$

where T is the sample duration.

(3) When $t = -\frac{v_{1x}}{v_1^2}x_1 - \frac{v_{1y}}{v_1^2}y_1 \in [0, T]$, we get:

$$\xi_{N_1}^2 = R_1^2 - \left(\frac{v_{1x}}{v_1}x_1 + \frac{v_{1y}}{v_1}y_1\right)^2. \quad (17)$$

(4) When $t = -\frac{v_{1x}}{v_1^2}x_1 - \frac{v_{1y}}{v_1^2}y_1 \in (-\infty, 0) \cup (T, \infty)$, take any $t = t_1 \in [0, T]$, we get:

$$\xi_{N_1}^2 = v_1^2 t_1^2 + 2(x_1 v_{1x} + y_1 v_{1y})t_1 + R_1^2. \quad (18)$$

In addition, the squared velocity curve of the head node is:

$$\chi_{N_1}^2 = V_{\text{He}}^2 = v_{1x}^2 + v_{1y}^2 + \omega'^2(t). \quad (19)$$

Consider that the derivative of the micro-undulation movement is extremely small, we get:

$$\Rightarrow \chi_{N_1}^2 \approx v_{1x}^2 + v_{1y}^2, \quad (20)$$

in which the principle component is constant, so only one point is enough.

1.2. Torso Node N_2

Similarly, for the torso node, the analysis process is exactly the same as for the head node.

Here, define R_2 to replace R_1 :

$$R_2 = \sqrt{x_1^2 + y_1^2 + \left(\frac{h_1 + h_2}{2} - h_0\right)^2}. \quad (21)$$

Thus, the squared one-way propagation distance $\xi_{N_2}^2$ is:

$$\xi_{N_2}^2 = v_1^2 t^2 + 2(x_1 v_{1x} + y_1 v_{1y})t + R_2^2, \quad (22)$$

which is also a quadratic function with respect to t . The effect of wall refraction on the distance curve is still the addition of a $d(\sqrt{\epsilon_r} - 1)$ term, which does not affect the order of the curve. (It will also not be considered subsequently.) Thus, three different points are enough. In addition, the squared velocity curve of torso node $\chi_{N_2}^2$ is the same as the head node:

$$\begin{aligned} \chi_{N_2}^2 &= \chi_{N_1}^2 = V_{\text{He}}^2 \\ &= v_{1x}^2 + v_{1y}^2 + \omega'^2(t), \end{aligned} \quad (23)$$

$$\Rightarrow \chi_{N_2}^2 \approx v_{1x}^2 + v_{1y}^2. \quad (24)$$

According to the above analysis, only one point is needed to reconstruct the original function.

1.3. Hand Nodes N_3 & N_4

Assume that the human arm is a radial rigid body. In the sinusoidal pendulum model, the maximum angle between the swinging arm and the vertical direction is θ_1 . Similarly its squared one-way propagation distance curve is:

$$\begin{aligned} \xi_{N_3}^2 &= R_3^2 + 2x_1 v_{1x} t + 2y_1 v_{1y} t + v_1^2 t^2 \\ &+ \frac{2l_1}{v_1} l_1 \sin(\theta_1 \sin(\varphi t))(x_1 v_{1x} + y_1 v_{1y} + v_1^2 t), \\ &- 2h_1 l_1 \cos(\theta_1 \sin(\varphi t)) \end{aligned} \quad (25)$$

where:

$$R_3 = \sqrt{x_1^2 + y_1^2 + h_1^2 + l_1^2}. \quad (26)$$

The term $\sin(\theta_1 \sin(\varphi t))$ is an odd, periodic, and bounded function, with a maximum value of $\sin(\theta_1)$, which can be uniquely determined by six points. Thus, in order to reconstruct the information in $\xi_{N_3}^2$, it is necessary to identify six points:

(1) When $t = 0$, we get:

$$\xi_{N_3}^2 = R_3^2 - 2h_1l_1 = x_1^2 + y_1^2 + (h_1 - l_1)^2 \quad (27)$$

(2) When $t = T$, we get:

$$\begin{aligned} \xi_{N_3}^2 &= R_3^2 + 2x_1v_{1x}T + 2y_1v_{1y}T + v_1^2T^2 \\ &+ \frac{2l_1}{v_1}l_1 \sin(\theta_1 \sin(\varphi T))(x_1v_{1x} + y_1v_{1y} + v_1^2T) \\ &- 2h_1l_1 \cos(\theta_1 \sin(\varphi T)) \end{aligned} \quad (28)$$

(3) When $t \in (0, T)$, considering the following derivation that characterizes the monotonicity of the curve:

$$\begin{aligned} \frac{\partial \xi_{N_3}^2}{\partial t} &= 2R_4(t) \\ &+ 2R_4(t) \frac{l_1\theta_1\varphi}{v_1} \cos(\varphi t) \cos(\theta_1 \sin(\varphi t)) \\ &+ 2l_1 \sin(\theta_1 \sin(\varphi t))(v_1 + h_1\theta_1\varphi \cos(\varphi t)) \end{aligned} \quad (29)$$

in which:

$$R_4(t) = x_1v_{1x} + y_1v_{1y} + v_1^2t, \quad (30)$$

is not a constant function. If the zeros of Eq. (29) in $(0, T)$ are greater than or equal to 4, then the corresponding $t_1 \sim t_4$ in $\frac{\partial \xi_{N_3}^2}{\partial t_i} |_{i=1 \sim 4} = 0$ are the rest four points we need. If the zeros of Eq. (29) in $(0, T)$ are less than 4, then we continue by choosing the second-order derivative zeros as the desired t value. In the vast majority of cases, human gait habits usually satisfy:

$$\frac{T\varphi}{\pi} \geq 2, \quad (31)$$

which means:

$$T \geq \frac{2\pi}{\min(\varphi)}. \quad (32)$$

It is usually only necessary to use at most the second-order derivative zeros to pick the remaining four t values.

The squared velocity curve of the hand node N_3 is constructed using the vertex velocity of a sinusoidal pendulum:

$$\begin{aligned} \chi_{N_3}^2 &= V_{Ha}^2 \\ &= v_1^2 - 2l_1v_1\theta_1\varphi \cos(\varphi t) \cos(\theta_1 \sin(\varphi t)) \\ &+ l_1^2\theta_1^2\varphi^2 \cos^2(\varphi t) \end{aligned} \quad (33)$$

According to the above analysis, five different points are needed to reconstruct the original function:

(1) When $t = 0$, we get:

$$V_{Ha}^2 = (v_1 - l_1\theta_1\varphi)^2. \quad (34)$$

(2) When $t = T$, we get:

$$\begin{aligned} V_{Ha}^2 &= v_1^2 - 2l_1v_1\theta_1\varphi \cos(\varphi T) \cos(\theta_1 \sin(\varphi T)) \\ &+ l_1^2\theta_1^2\varphi^2 \cos^2(\varphi T) \end{aligned} \quad (35)$$

(3) When $t \in (0, T)$, consider the following derivation:

$$\begin{aligned} \frac{\partial V_{Ha}^2}{\partial t} &= 2l_1v_1\theta_1\varphi^2 \sin(\varphi t) \cos(\theta_1 \sin(\varphi t)) \\ &+ 2l_1v_1\theta_1^2\varphi^2 \cos^2(\varphi t) \sin(\theta_1 \sin(\varphi t)) \\ &- 2l_1^2\theta_1^3\varphi^3 \sin(\varphi t) \cos(\varphi t) \end{aligned} \quad (36)$$

We take t_i in $\frac{\partial V_{Ha}^2}{\partial t_i} |_{i=1 \sim 3} = 0$ for the rest selection of t value. If there are not enough extreme points, the remaining t_i are selected by second derivative zeros $\frac{\partial^2 V_{Ha}^2}{\partial t_i^2} = 0$.

For hand node N_4 , the squared distance curve can be expressed as the transformation of $\xi_{N_3}^2$ by π phase:

$$\begin{aligned} \xi_{N_4}^2 &= R_3^2 + 2x_1v_{1x}t + 2y_1v_{1y}t + v_1^2t^2 \\ &+ \frac{2l_1}{v_1}l_1 \sin(\theta_1 \sin(\varphi t) + \pi)(x_1v_{1x} + y_1v_{1y} + v_1^2t) \\ &- 2h_1l_1 \cos(\theta_1 \sin(\varphi t) + \pi) \end{aligned} \quad (37)$$

The squared velocity curve of the hand node N_4 is :

$$\begin{aligned} \chi_{N_4}^2 &= v_1^2 - 2l_1v_1\theta_1\varphi \cos(\varphi t) \cos(\theta_1 \sin(\varphi t) + \pi) \\ &+ l_1^2\theta_1^2\varphi^2 \cos^2(\varphi t) \end{aligned} \quad (38)$$

Therefore, six and five different points are needed to reconstruct the squared distance and velocity curves, respectively.

Algorithm 1: Generation of Range and T-F Profiles

Input: $\mathbf{I}_r = \mathbf{RTM}$, $\mathbf{I}_d = \mathbf{DTM}$

Output: Range and T-F profiles $\mathbf{R}^2\mathbf{TM}$, $\mathbf{D}^2\mathbf{TM}$ after vertical axis squaring.

```
[s, l] = size( $\mathbf{I}_r^\top$ ), [p, q] = size( $\mathbf{I}_d^\top$ ),  $i = j = k = 0$ ;
/* size() denotes the dimension of the matrix. */
 $\mathbf{I}_{r,2} = \text{zeros}(s, l^2)$ ;
/* zeros() is to create an all-zero matrix. */
if  $q \equiv 2 \pmod{2}$  then
     $\mathbf{I}_{d,1} = \mathbf{I}_{d,2} = \text{zeros}(p, q^2/4)$ ;
else
     $\mathbf{I}_{d,1} = \mathbf{I}_{d,2} = \text{zeros}(p, (q+1)^2/4)$ ;
end
end
for  $i = 1 : s$  do
    for  $j = 1 : l$  do
        for  $k = 1 : (2j-1)$  do
             $\mathbf{I}_{r,2}(i, (j-1)^2 + k) = \mathbf{I}_r^\top(i, j)$ ;
        end
    end
end
end
for  $i = 1 : p$  do
    for  $j = 1 : \lfloor \frac{q}{2} \rfloor + 1$  do
        for  $k = 1 : (2j-1)$  do
             $\mathbf{I}_{d,1}(i, (j-1)^2 + k) = \mathbf{I}_d^\top(i, [q/2] - j)$ ;
             $\mathbf{I}_{d,2}(i, (j-1)^2 + k) = \mathbf{I}_d^\top(i, [q/2] + j)$ ;
        end
    end
end
end
 $\mathbf{R}^2\mathbf{TM} = \text{Norm}(\mathbf{I}_{r,2}^\top)$ ;
 $\mathbf{D}^2\mathbf{TM} = \text{Norm}(\text{Con}(\text{flip}(\mathbf{I}_{d,1}), \mathbf{I}_{d,2})^\top)$ ;
/* Norm() is the normalization function, flip()
means flip the matrix vertically, and Con()
means the concatenation of two matrices. */
```

1.4. Foot Nodes N_5 & N_6

The analysis process for the foot nodes is exactly the same as the hand nodes, and only the definition of some parameters

TABLE III
CALCULATION OF MINIMUM NUMBER OF CORNER POINTS IN RANGE AND T-F PROFILES*.

Motion	Nodes	Curve Equations on R ² TM	Curve Equations on D ² TM	MNCP (R ² TM)	MNCP (D ² TM)
Mot. 1 ¹	N ₁	$R_{N_1,t}^2 = a_{N_1,0} + a_{N_1,1}t + a_{N_1,2}t^2$	$D_{N_1,t}^2 = b_{N_1,0}$	3	1
	N ₂	$R_{N_2,t}^2 = a_{N_2,0} + a_{N_2,1}t + a_{N_2,2}t^2$	$D_{N_2,t}^2 = b_{N_2,0}$	3	1
	N ₃	$R_{N_3,t}^2 = (a_{N_3,0} + a_{N_3,1} \sin(a_{N_3,2} \sin(a_{N_3,3}t)))$	$D_{N_3,t}^2 = b_{N_3,0}$	6	5
		$\cdot (a_{N_3,4} + a_{N_3,5}t + a_{N_3,6}t^2)$	$+ b_{N_3,1} \cos^2(b_{N_3,2}t)$		
	N ₄	$R_{N_4,t}^2 = (a_{N_4,0} + a_{N_4,1} \sin(a_{N_4,2} \sin(a_{N_4,3}t)))$	$+ b_{N_3,3} \cos(b_{N_3,4}t) \cos(b_{N_3,5} \sin(b_{N_3,6}t))$	6	5
		$\cdot (a_{N_4,4} + a_{N_4,5}t' + a_{N_4,6}t'^2)$	$+ b_{N_4,1} \cos^2(b_{N_4,2}t')$		
	N ₅	$R_{N_5,t}^2 = (a_{N_5,0} + a_{N_5,1} \sin(a_{N_5,2} \sin(a_{N_5,3}t)))$	$+ b_{N_4,3} \cos(b_{N_4,4}t') \cos(b_{N_4,5} \sin(b_{N_4,6}t'))$	6	5
		$\cdot (a_{N_5,4} + a_{N_5,5}t' + a_{N_5,6}t'^2)$	$+ b_{N_5,1} \cos^2(b_{N_5,2}t')$		
	N ₆	$R_{N_6,t}^2 = (a_{N_6,0} + a_{N_6,1} \sin(a_{N_6,2} \sin(a_{N_6,3}t)))$	$+ b_{N_5,3} \cos(b_{N_5,4}t') \cos(b_{N_5,5} \sin(b_{N_5,6}t'))$	6	5
		$\cdot (a_{N_6,4} + a_{N_6,5}t + a_{N_6,6}t^2)$	$+ b_{N_6,1} \cos^2(b_{N_6,2}t)$		
	Total	$R_t^2 = \sum_{i=1}^6 R_{N_i,t}^2$	$+ b_{N_6,3} \cos(b_{N_6,4}t) \cos(b_{N_6,5} \sin(b_{N_6,6}t))$	30	22
			$D_t^2 = \sum_{i=1}^6 D_{N_i,t}^2$		
Mot. 2 ¹	N ₁	$R_{N_1,t}^2 = a'_{N_1,0} + a'_{N_1,1} \sin(a'_{N_1,2}t'')$	$D_{N_1,t}^2 = b'_{N_1,0} + b'_{N_1,1} \cos(b'_{N_1,2}t'')$	5	5
	N ₂	$R_{N_2,t}^2 = a'_{N_2,0} + a'_{N_2,1} \sin(a'_{N_2,2}t'')$	$D_{N_2,t}^2 = b'_{N_2,0} + b'_{N_2,1} \cos(b'_{N_2,2}t'')$	5	5
	N ₃	$R_{N_3,t}^2 = a'_{N_3,0} + a'_{N_3,1} \sin(a'_{N_3,2}t'')$	$D_{N_3,t}^2 = b'_{N_3,0} + b'_{N_3,1} \cos(b'_{N_3,2}t'')$	5	5
	N ₄	$R_{N_4,t}^2 = a'_{N_4,0} + a'_{N_4,1} \sin(a'_{N_4,2}t'')$	$D_{N_4,t}^2 = b'_{N_4,0} + b'_{N_4,1} \cos(b'_{N_4,2}t'')$	5	5
	N ₅	$R_{N_5,t}^2 = a'_{N_5,0} + a'_{N_5,1} \sin(a'_{N_5,2}t'')$	$D_{N_5,t}^2 = b'_{N_5,0} + b'_{N_5,1} \cos(b'_{N_5,2}t'')$	5	5
	N ₆	$R_{N_6,t}^2 = a'_{N_6,0} + a'_{N_6,1} \sin(a'_{N_6,2}t'')$	$D_{N_6,t}^2 = b'_{N_6,0} + b'_{N_6,1} \cos(b'_{N_6,2}t'')$	5	5
	Total	$R_t^2 = \sum_{i=1}^6 R_{N_i,t}^2$	$D_t^2 = \sum_{i=1}^6 D_{N_i,t}^2$	30	30

* All the modulus in this table, including $a_{N_i,j}, b_{N_i,j}, a'_{N_i,j}, b'_{N_i,j}, i \in \mathcal{N}, j \in \mathcal{N}$ are constants related to the human body posture and gait parameters that are independent of time t . $t' = t - \pi$, $t'' = t - t_0$, where t_0 is a quarter cycle of the previously defined motion without position change. $N_1 \sim N_6$ are consistent with the definition in Fig. 2. $R_{N_i,t}^2, D_{N_i,t}^2, i = 1 \sim 6$ represent the vertical axis in R²TM and D²TM, respectively.

¹ Mot. 1 and Mot. 2 denote the natural walking and in-situ acceleration discussed in section II, respectively.

needs to be modified. For example, replace l_1, h_1, θ_1 with l_2, h_2, θ_2 , respectively. It can be concluded:

$$\begin{aligned} \xi_{N_5}^2 &= R_5^2 + 2x_1v_{1x}t + 2y_1v_{1y}t + v_1^2t^2 \\ &+ \frac{2l_2}{v_1}l_2 \sin(\theta_2 \sin(\varphi t))(x_1v_{1x} + y_1v_{1y} + v_1^2t), \\ &- 2h_2l_2 \cos(\theta_2 \sin(\varphi t)) \end{aligned} \quad (39)$$

$$\begin{aligned} \xi_{N_6}^2 &= R_5^2 + 2x_1v_{1x}t + 2y_1v_{1y}t + v_1^2t^2 \\ &+ \frac{2l_2}{v_1}l_2 \sin(\theta_2 \sin(\varphi t) + \pi)(x_1v_{1x} + y_1v_{1y} + v_1^2t), \\ &- 2h_2l_2 \cos(\theta_2 \sin(\varphi t) + \pi) \end{aligned} \quad (40)$$

where:

$$R_5 = \sqrt{x_1^2 + y_1^2 + h_2^2 + l_2^2}, \quad (41)$$

and:

$$\begin{aligned} \chi_{N_5}^2 &= v_1^2 - 2l_2v_1\theta_2\varphi \cos(\varphi t) \cos(\theta_2 \sin(\varphi t)) \\ &+ l_2^2\theta_2^2\varphi^2 \cos^2(\varphi t), \end{aligned} \quad (42)$$

$$\begin{aligned} \chi_{N_6}^2 &= v_1^2 - 2l_2v_1\theta_2\varphi \cos(\varphi t) \cos(\theta_2 \sin(\varphi t) + \pi) \\ &+ l_2^2\theta_2^2\varphi^2 \cos^2(\varphi t). \end{aligned} \quad (43)$$

In total, six and five different points are needed to reconstruct the squared distance and velocity curves, respectively.

2. In-situ Acceleration

The body of the human can be modeled solely by upper torso node located at height h_1 . Then:

$$h_1 = \frac{1}{2} \left(\Delta h_1 \sin(t - t_0) + h_1 - \frac{1}{2} \Delta h_1 \right), \quad (44)$$

where t_0 is the half period of the in-situ acceleration motion, $T = 4t_0$, Δh_1 is the maximum height variation for the upper torso node. Thus, the squared one-way propagation distance curve ξ^2 at this moment can be rewritten as:

$$\begin{aligned} \xi^2 &= R_6^2 + \frac{1}{8} \Delta h_1^2 + \Delta h_1 R_6' \sin \frac{\pi}{2t_0} (t - t_0) \\ &- \frac{1}{8} \Delta h_1^2 \cos \frac{\pi}{t_0} (t - t_0) \end{aligned} \quad (45)$$

where:

$$R_6' = h_1 - h_0 - \frac{1}{2} \Delta h_1, \quad (46)$$

$$R_6 = \sqrt{x_1^2 + y_1^2 + R_6'^2}. \quad (47)$$

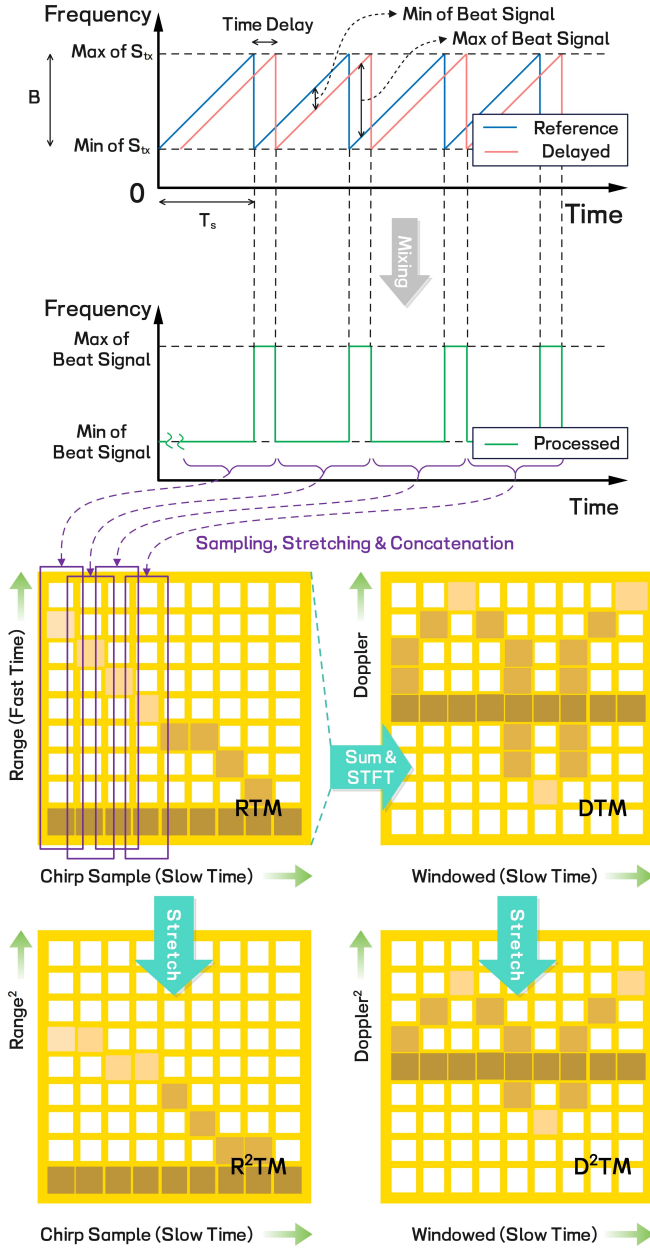


Fig. 3. Principle of LFM CW signal transmitting, receiving, sampling, and time-frequency analysis.

The orders of four parts in Eq. (45) are 0, 0, 5, 5, respectively.

Furthermore, the squared velocity curve of the upper torso node is:

$$V_{UT}^2 = \frac{\pi}{32t_0^2} \Delta h_1^2 \left(1 + \cos \frac{\pi}{t_0} (t - t_0) \right), \quad (48)$$

where the order of Eq. (48) is also 5. The resulting squared distance curves $\xi_i^2, i = N_1 \sim N_6$ and squared velocity curves $\chi_i^2, i = N_1 \sim N_6$ are obtained from ξ^2, V_{UT}^2 after stretching transformation in vertical axis, respectively. Therefore, 5 different points are needed to reconstruct both the squared distance and velocity curves, respectively.

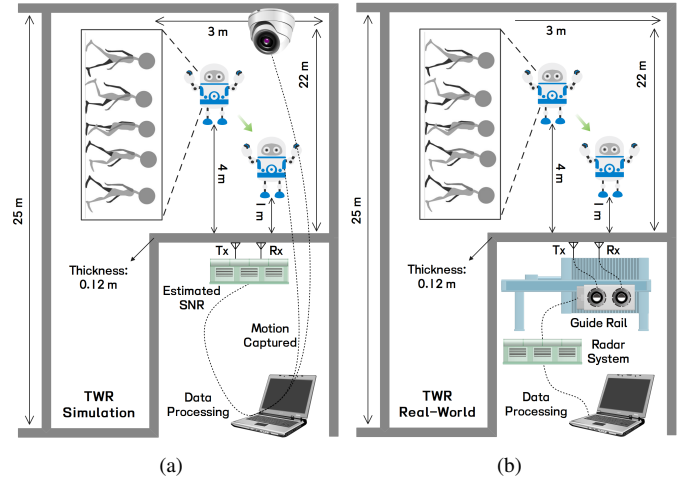


Fig. 4. Schematic diagrams of the experimental scenarios: (a) through-the-wall, simulation, and (b) through-the-wall, real-world measurement. The motion captured data in (a) comes from open source works, while (b) is from the prototype TWR system we built ourselves.

B. Minimum Number of Corners in Range and T-F Profiles

As shown in Fig. 3, to effectively display the micro-Doppler signature, the time-domain radar echoes are concatenated along the slow-time index m to form a two-dimensional data matrix. After performing clutter and noise suppression on the matrix, the RTM is obtained. The clutter suppression is achieved using MTI filter and the noise suppression is achieved using EMD algorithm [35]. By summing the data of all range cells in the RTM and utilizing STFT, a two-dimensional T-F image is obtained referred to as DTM [6]. The EMD algorithm is again used for clutter and noise residual suppression on the DTM [35]. From the analysis of the human motion model, it is found that the selection of points for reconstructing the complete information of the curves is related to the square of the range and velocity. Therefore, the RTM and DTM are stretched to square coordinates in vertical axes. The necessity lies in the fact that without this operation, the order of the resulting kinematic state curves for each limb node would change, and thus the minimum number of reconstruction corner points required would also change. The operation is achieved by interpolation, which finally outputs R^2TM, D^2TM . Detailed flow for generating R^2TM and D^2TM is shown in Algorithm 1.

The horizontal and vertical coordinates corresponding to R^2TM and D^2TM consist of the trajectory equation obtained in human motion modeling. Corners in blob form usually appear at locations on the images where the curvature of the trajectory is the largest.

Based on the results of the human motion model, the squared one-way propagation distance curves and squared velocity curves are summarized and rewritten for each scattering center on R^2TM and D^2TM in TABLE III. The minimum number of corner points required to reconstruct the complete information for each curve is calculated separately. For activities where the body's position changes, the minimum required number of corner points on R^2TM, D^2TM is 30 and 22, respectively. For activities where the body's position

TABLE IV
DETAILS OF THE EXPERIMENTS*.

Name of Validation Experiments		Interpretations
Modeling Theory	Visualization	Displaying radar images of the true label, simulated, and measured data with their corner representations
	Similarity	Calculating the similarity between the radar images, the corner representations, and the true values
	Robustness	Testing the similarity between corner representations and their truth values under different noise levels
Corner Representation Theory	Feature Embedding	Comparing the feature separation level before and after corner representation
	Generalization Capability	Using frontier classifiers to compare the generalization ability before and after corner representation
	Scenario Adaptation	Verifying the adaptation of the proposed method to inhomogeneous wall scenarios

* All these validations are analyzed in detail in subsections B and C of the experimental section.

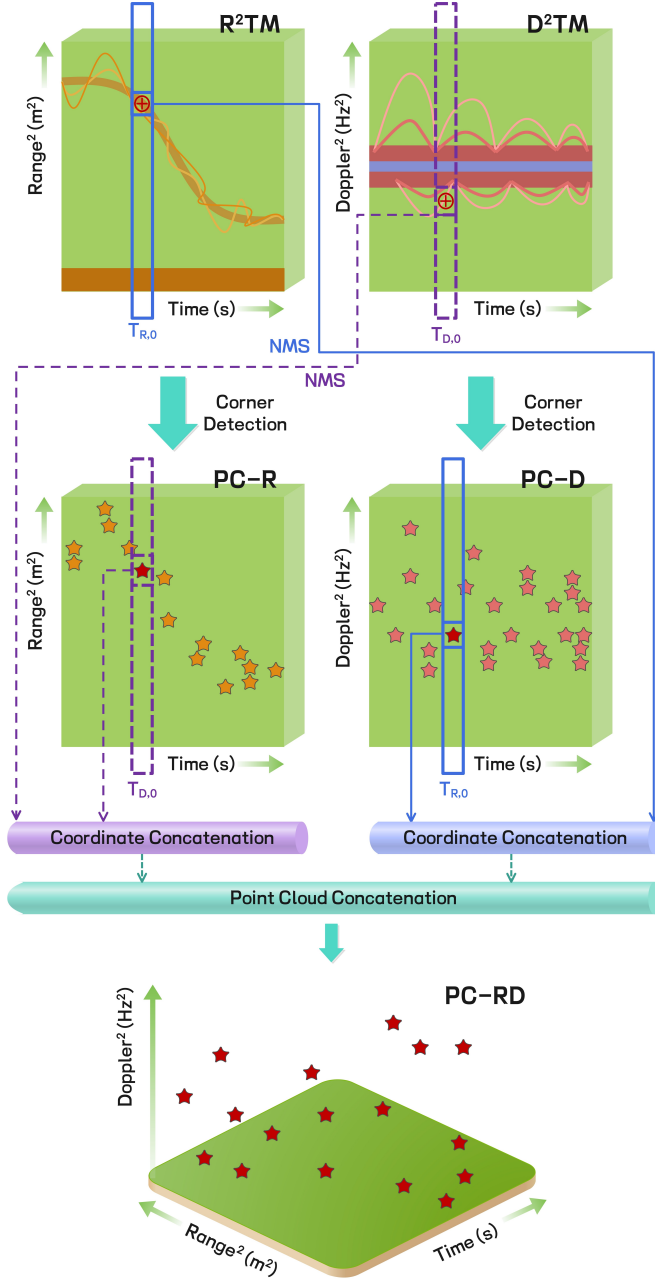


Fig. 5. Schematic diagram of the generation process of PC - RD.

does not change, the minimum required number of corner points on both R^2TM , D^2TM is 30. Consider the tolerance, and for ease of algorithm design, the number of corners is

TABLE V
UNIFORM PARAMETERS OF RADAR SYSTEM*.

Parameters	Value
Antenna Transceiver Spacing	(SISO) 0.15 m
Work Center Frequency	1.5 GHz
Band Width	2 GHz
Sampling Points ¹	1024
Sampling Period	4 s
Wall Thickness	0.12 m
Human Motion Range from Radar	1 ~ 4 m
SNR of Raw Data ²	-19.85 ~ -12.46 dB
SNR of Processed Data ²	≈ 0 dB
Antenna Height to Ground	1.5 m
Number of Activities ³	12

* For reasons of rigor, we unify the simulated and measured parameters.

¹ Both on fast-time and slow-time. Therefore the final generated time-domain echo matrix should be in square size.

² The SNR mentioned in the table are obtained by manually selecting the target's region of the image and calculating the image pixel energy [48].

³ The categories and the amount of data might not correspond in some datasets. Thus, we reselect and reorganize the labels from the original and introduce overlap window slicing to ensure consistency of the experiments.

selected as 30.

IV. EXPERIMENTAL VERIFICATION

In this section, the parameters of radar systems used for TWR HAR in both simulated and measured scenarios are first given, and the method for achieving feature extraction is explained. Then, as shown in TABLE IV, the correctness and effectiveness of the modeling theory and the corner representation theory are verified in sequence. Finally, a discussion of the directions that remain to be optimized for proposed theory is given.

A. Configuration of Radar System

As shown in TABLE V, parameters for the developed TWR systems are presented. Both simulation and real-world experiment data sets are collected for validation. In the following, the terms “Simulated” and “Measured” are used to refer to these two data sets, respectively. The radar is placed outdoors for indoor human detection. The height from radar antennas to the ground is 1.5 m. The center frequency is of 1.5 GHz with bandwidths of 2 GHz. The total number of fast time samples is 1024. the number of slow time samples is 256 per second, and the sampling time window is 4 seconds, thus the resulting one frame of radar data is a square matrix. The thickness

of both simulated and measured walls is 0.12 m, where an isotropic rectangle with a relative dielectric constant of 6 is used in simulated scenario instead. The range of indoor human activities is from 1 ~ 4 m. There are 12 human activities in total, including: S1, Empty; S2, Punching; S3, Kicking; S4, Grabbing; S5, Sitting Down; S6, Standing Up; S7, Rotating; S8, Walking; S9, Sitting to Walking; S10, Walking to Sitting; S11, Falling to Walking; S12, Walking to Falling. All the rest parameters are kept consistent for the two radar systems.

The two data collection scenarios are schematically shown in Fig. 4. For simulated scenario, the data set is referenced from related open source work from UCL [49]. The team utilizes the motion capture method to get the trajectory curves of the nodes of the human body during various activities. Based on the team's data, the locations of each limb node at specific moments are obtained. The limb nodes are populated with isotropic homogeneous ellipsoids to generate radar echoes under through-the-wall scene using low-frequency UWB transceiver. To standardize the activity categories and sampling time window lengths, the datas generated from the public dataset are re-selected and re-sliced [50].

For measured scenario, the data set is obtained by the experimental prototype of the TWR built in [35] with the parameters described above. The interpretability of the data is improved by pre-processing operations such as standards-based channel calibration. Similar to the operation of the simulated data set, to standardize the activity categories and sampling time window lengths, the datas collected are re-selected and re-sliced.

In the following simulated and measured experiments, the SOGGDD filtering is used uniformly for blob-sensitive micro-Doppler corner detection on both $\mathbf{R}^2\text{TM}$ and $\mathbf{D}^2\text{TM}$ [51]. Define the point cloud data matrices obtained from corner detection using SOGGDD filtering on $\mathbf{R}^2\text{TM}$ and $\mathbf{D}^2\text{TM}$ as $\mathbf{PC} - \mathbf{R}$ and $\mathbf{PC} - \mathbf{D}$, respectively. Then, $\mathbf{PC} - \mathbf{R}$ and $\mathbf{PC} - \mathbf{D}$ are fused together to obtain a three-dimensional point cloud, which is used as the final extracted micro-Doppler signature. As shown in Fig. 5, take a corner point on one of the slow time of the $\mathbf{PC} - \mathbf{R}$ and find the point of maximum amplitude on $\mathbf{D}^2\text{TM}$ for the data corresponding to the same slow time. This frequency coordinate is concatenated to the corner point on the $\mathbf{PC} - \mathbf{R}$ to obtain a 3D coordinate. Similarly, take a corner point on one of the slow time of the $\mathbf{PC} - \mathbf{D}$ and find the point of maximum amplitude on $\mathbf{R}^2\text{TM}$ for the data corresponding to the same slow time. This frequency coordinate is concatenated to the corner point on the $\mathbf{PC} - \mathbf{D}$ to obtain a 3D coordinate. Iterating through both $\mathbf{PC} - \mathbf{R}$ and $\mathbf{PC} - \mathbf{D}$ and concatenating all the 3D coordinates into a matrix, which obtains the desired micro-Doppler corner point cloud representation $\mathbf{PC} - \mathbf{RD}$ with the dimension of 60×3 .

B. Validation of Modeling Theory: Visualization, Similarity, and Robustness

The visualizations of our proposed micro-Doppler corner representation on two different types of TWR data are shown in Fig. 7 and Fig. 8, while the groundtruth maps generated

using the reference trajectories of human motion obtained from the captured datas are shown in Fig. 6. Fig. 7 gives the results for simulated scenario, and Fig. 8 gives the results for measured scenario. Comparing Fig. 7 and Fig. 8 with Fig. 6 can be a viable option for evaluating the effectiveness of the proposed model and feature representation method.

As shown in Fig. 7, regardless of the type of activity, human motion simultaneously induces Doppler and micro-Doppler effects on both the generated $\mathbf{R}^2\text{TM}$ and $\mathbf{D}^2\text{TM}$. In Fig. 8, the Doppler and micro-Doppler signature tends to be much weaker, but still visible from the image results. The Doppler signature on the $\mathbf{R}^2\text{TM}$ is the overall trend of displacement of the nodes of the human body. The micro-Doppler signature, on the other hand, is the presence of micro-motion of the nodes of the body with respect to each other, which in turn results in the appearance of multiple peaks on or within the curve envelope. On the $\mathbf{D}^2\text{TM}$, the Doppler signature is the curves that are not axisymmetric or centrosymmetric. In contrast, the micro-Doppler signature is the appearance of peaks that are relatively weak in energy but have much higher frequencies. All these image features are used for corner representation.

Compared the $\mathbf{R}^2\text{TM}$ with groundtruth in both simulated and measured scenarios, it can be seen that the macroscopic motion trends of human limb nodes in the resulting images are basically the same. Compared $\mathbf{D}^2\text{TM}$ with groundtruth, it can be clearly seen that the relative motion trends of human limb nodes in the resulting images are basically the same.

The Doppler and micro-Doppler signature on the images acquired in simulated scenario are more obvious. The images acquired in measured scenario are even lower in SNR and resolution, which means that both Doppler and micro-Doppler signature are blurred. However, after corner extraction, both Doppler and micro-Doppler signature are well represented.

In order to quantitatively assess that the corner representation do reflect the Doppler and micro-Doppler signature in both the $\mathbf{R}^2\text{TM}$ and $\mathbf{D}^2\text{TM}$, fully resolved earth mover's distance is introduced to measure the variability between two point clouds [52]. The earth mover's distance metric E - M - Dist of the $\mathbf{PC} - \mathbf{R}$ and $\mathbf{PC} - \mathbf{D}$ is:

$$\text{E-M-Dist}(\mathbf{GT}, \mathbf{Ta}) = \frac{\sum_{i=1}^{\zeta} \sum_{j=1}^{\zeta'} \mathbf{fp}_{ij} \mathbf{Dp}_{ij}}{\sum_{i=1}^{\zeta} \sum_{j=1}^{\zeta'} \mathbf{fp}_{ij}}, \quad (49)$$

where $\zeta = \zeta' = 30$. $\mathbf{fp} = [\mathbf{fp}_{ij}]$, $\mathbf{fp}_{ij} \geq 0$, $1 \leq i \leq \zeta$, $1 \leq j \leq \zeta'$ is the corresponding weights, which can be obtained by solving:

$$F_p = \arg \max_{F_p} \left(\sum_{i=1}^{\zeta} \sum_{j=1}^{\zeta'} \mathbf{fp}_{ij} \mathbf{Dp}_{ij} \right), \quad (50)$$

which satisfies the constraints below:

$$\sum_{j=1}^{\zeta'} \mathbf{fp}_{ij} \leq \text{GT}_{\text{po}_i}, \quad 1 \leq i \leq \zeta, \quad (51)$$

$$\sum_{i=1}^{\zeta} \mathbf{fp}_{ij} \leq \text{Ta}_{\text{po}'_j}, \quad 1 \leq j \leq \zeta', \quad (52)$$

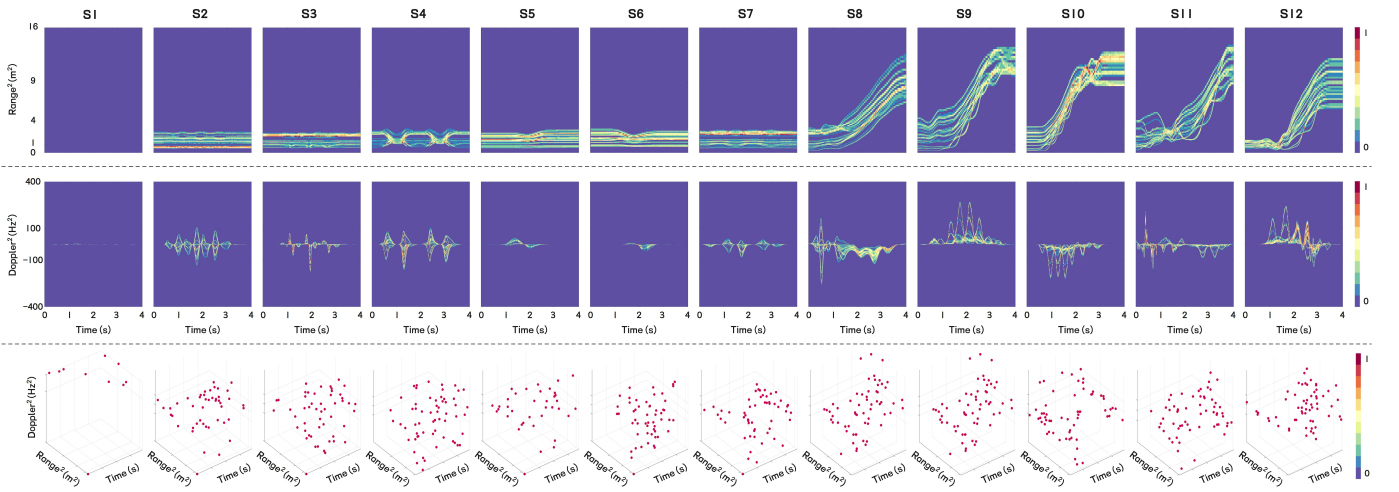


Fig. 6. Visualization of groundtruth under 12 human activities: The first row shows the $\mathbf{R}^2\mathbf{T}\mathbf{M}$ images, the second row shows the $\mathbf{D}^2\mathbf{T}\mathbf{M}$ images, and the third row shows the obtained micro-Doppler corner representation $\mathbf{PC} - \mathbf{RD}$. Activity labels include: $S1$, Empty; $S2$, Punching; $S3$, Kicking; $S4$, Grabbing; $S5$, Sitting Down; $S6$, Standing Up; $S7$, Rotating; $S8$, Walking; $S9$, Sitting to Walking; $S10$, Walking to Sitting; $S11$, Falling to Walking; $S12$, Walking to Falling.

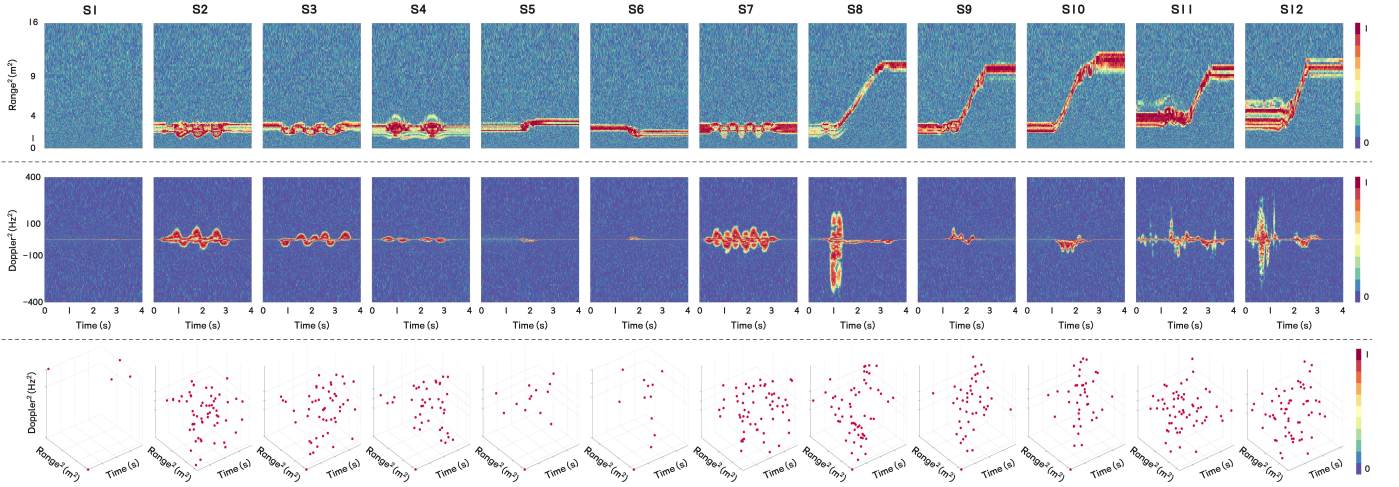


Fig. 7. Visualization of simulated datas under 12 human activities: The first row shows the $\mathbf{R}^2\mathbf{T}\mathbf{M}$ images, the second row shows the $\mathbf{D}^2\mathbf{T}\mathbf{M}$ images, and the third row shows the obtained micro-Doppler corner representation $\mathbf{PC} - \mathbf{RD}$. $S1 - S12$ are consistent with the definition in Fig. 6.

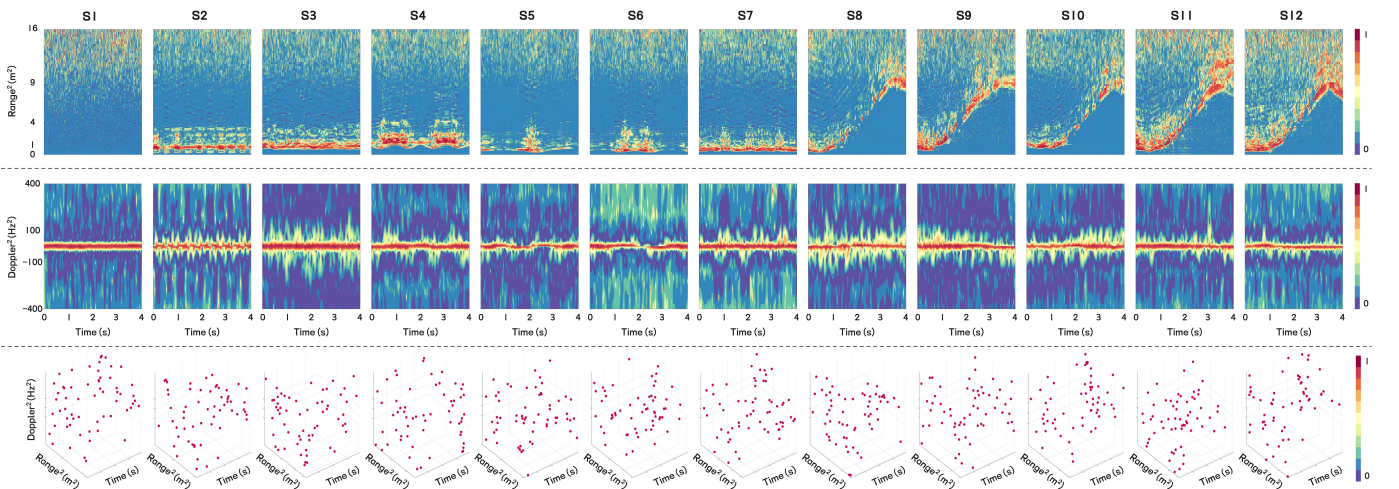


Fig. 8. Visualization of measured datas under 12 human activities: The first row shows the $\mathbf{R}^2\mathbf{T}\mathbf{M}$ images, the second row shows the $\mathbf{D}^2\mathbf{T}\mathbf{M}$ images, and the third row shows the obtained micro-Doppler corner representation $\mathbf{PC} - \mathbf{RD}$. $S1 - S12$ are consistent with the definition in Fig. 6.

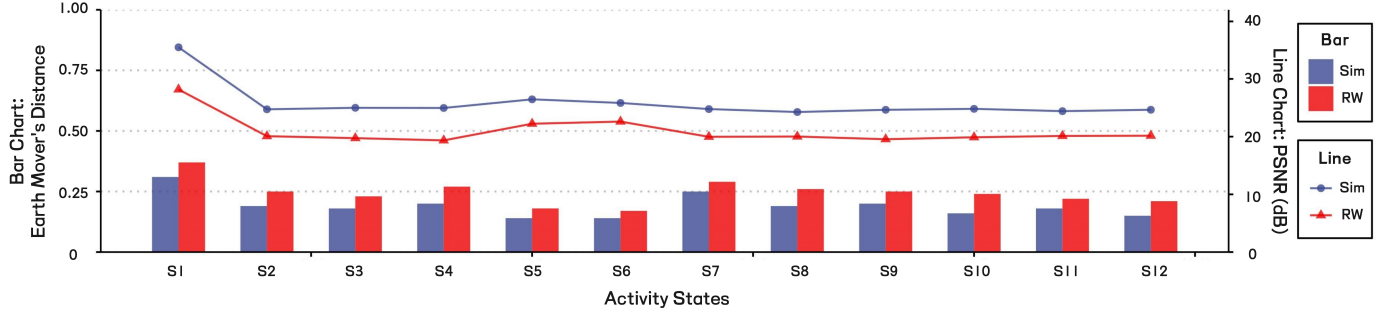


Fig. 9. PSNR of the two types of R^2TM versus groundtruth, and the earth mover's distance of the corner representation versus the groundtruth point cloud. "Sim" is the abbreviation of "Simulated". "RW" is the abbreviation of "Real-World Measured". The remaining definitions are consistent with Fig. 6.

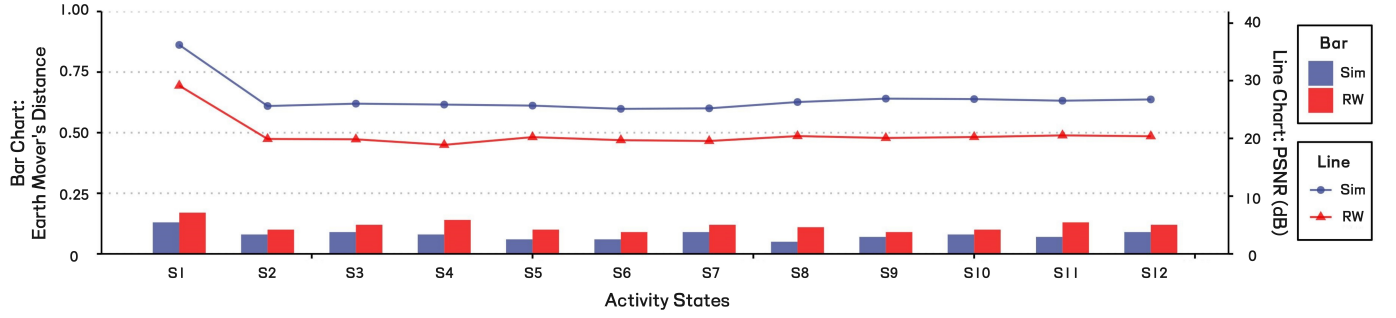


Fig. 10. PSNR of the two types of D^2TM versus groundtruth, and the earth mover's distance of the corner representation versus the groundtruth point cloud. "Sim" is the abbreviation of "Simulated". "RW" is the abbreviation of "Real-World Measured". The remaining definitions are consistent with Fig. 6.

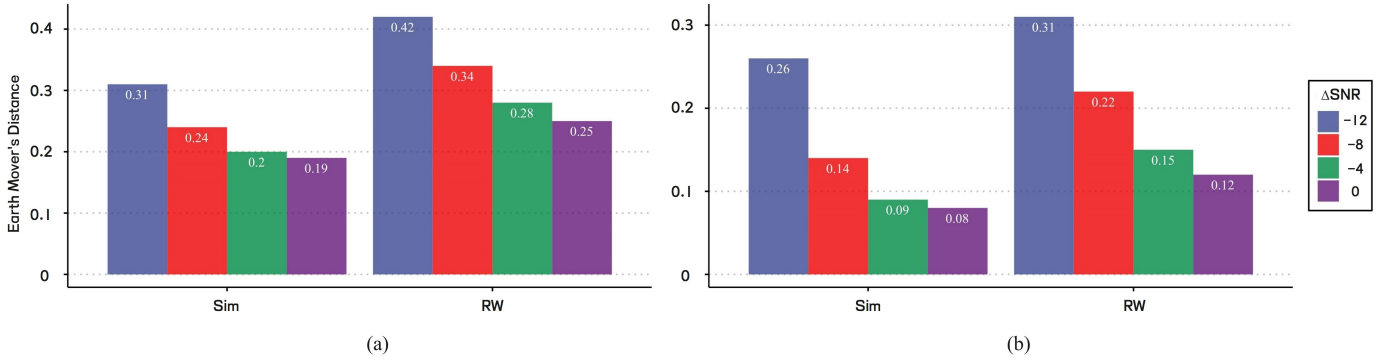


Fig. 11. Robustness test of corner representations at different noise levels, where (a) is on R^2TM and (b) is on D^2TM . ΔSNR is the value of SNR decreasing in dB unit when adding different power of Gaussian noise manually. "Sim" is the abbreviation of "Simulated". "RW" is the abbreviation of "Real-World Measured". The remaining definitions are consistent with Fig. 6.

$$\sum_{i=1}^{\zeta} \sum_{j=1}^{\zeta'} fp_{ij} = \min \left(\sum_{i=1}^{\zeta} GT_{po_i}, \sum_{j=1}^{\zeta'} Ta_{po'_j} \right), \quad (53)$$

where the groundtruth point cloud is:

$$GT = \{(po_1, GT_{po_1}), \dots, (po_{\zeta}, GT_{po_{\zeta}})\}, \quad (54)$$

and the target point cloud is:

$$Ta = \{(po'_1, Ta_{po'_1}), \dots, (po'_{\zeta'}, GT_{po'_{\zeta'}})\}, \quad (55)$$

where (po_i, GT_{po_i}) , $1 \leq i \leq \zeta$ and $(po'_j, Ta_{po'_j})$, $1 \leq j \leq \zeta'$ are normalized coordinates. The distance matrix is defined as $Dp = [Dp_{ij}]$, where Dp_{ij} denotes the Euclidean

distance between point (po_i, GT_{po_i}) and point $(po'_j, Ta_{po'_j})$. The unit of E-M-Dist is pixel 1. In [53], if the earth mover's distance is less than 1, it proves that the data is valid. If the earth mover's distance is less than 0.5, it proves that the point cloud possesses similarity. If the earth mover's distance is less than 0.25 for the vast majority of the data, it proves that the method has a good performance.

Fig. 9 and 10 give the earth mover's distance and PSNR results under different human activities. The calculation of PSNR on radar images can be found in paper [33]. The barchart denotes the earth mover's distance versus 12 human activities in unit 1, which locates on the left side of the vertical axis. The linechart denotes the PSNR versus 12 human activities in unit dB [54], which locates on the right side of

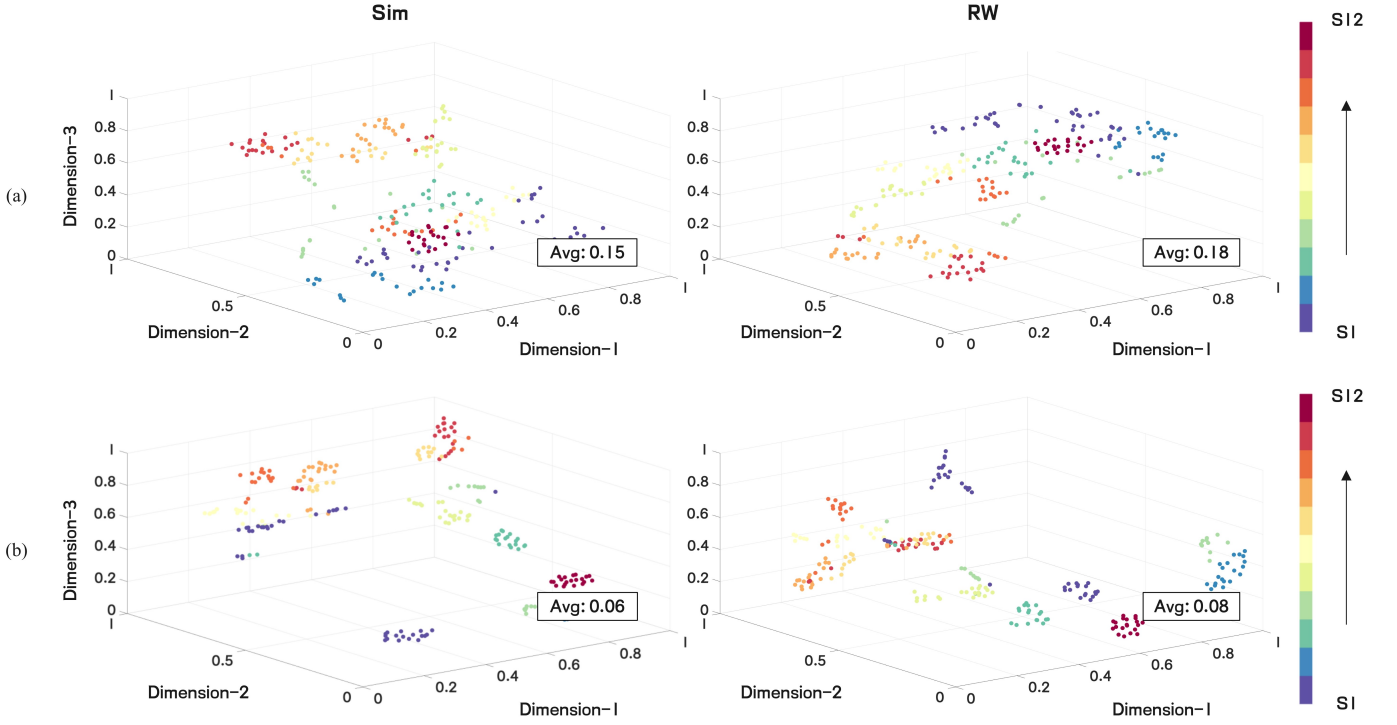


Fig. 12. Results of T-SNE analysis on R^2TM , where (a) is before corner representation, (b) is after corner representation. “Avg” is the abbreviation of “average distance from the center of clustering”. “Sim” is the abbreviation of “Simulated”. “RW” is the abbreviation of “Real-World Measured”.

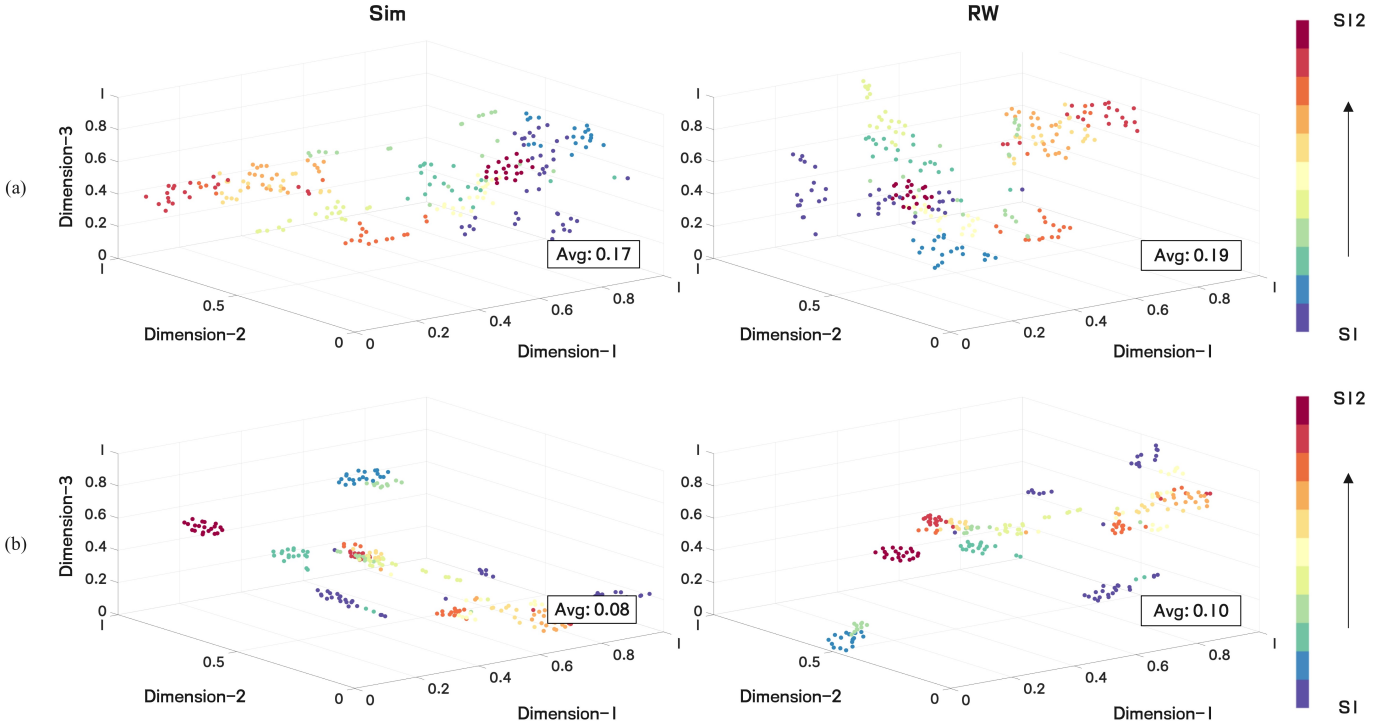


Fig. 13. Results of T-SNE analysis on D^2TM , where (a) is before corner representation, (b) is after corner representation. “Avg” is the abbreviation of “average distance from the center of clustering”. “Sim” is the abbreviation of “Simulated”. “RW” is the abbreviation of “Real-World Measured”.

the vertical axis.

From the results, for the group of empty scene ($S1$), both two types of R^2TM or D^2TM are relatively close to the groundtruth. These profiles do not exhibit any Doppler

or micro-Doppler signature associated with human motion. Therefore, there is a relatively large disparity in the corner representation. For the other 11 categories of activities, the earth mover’s distance of the corner representation to the

TABLE VI

COMPARISON OF THE IMPACT ON THE GENERALIZATION CAPABILITY OF BACK-END RECOGNITION MODELS ON NEW TESTERS' DATA BEFORE AND AFTER CORNER REPRESENTATION*.

(%)	Sim				RW			
	Tr	Va	Te1	Te2	Tr	Va	Te1	Te2
Methods Before Corner Representation								
M1 ¹	95.41	94.00	80.50	75.75	91.66	91.25	81.75	71.25
M2 ²	95.44	92.00	79.50	71.25	90.28	85.75	77.00	70.50
M3 ³	90.84	85.63	74.00	65.50	88.47	79.38	74.75	60.25
M4 ⁴	98.97	94.13	80.00	72.25	97.72	92.88	80.50	66.25
★ Methods After Corner Representation ★								
M1 ¹	93.22	90.63	88.00	82.25	92.84	90.13	86.50	80.25
M2 ²	96.78	93.38	90.50	84.75	93.34	87.63	83.50	80.00
M3 ³	93.91	90.75	86.50	81.00	90.44	84.63	79.75	71.25
M4 ⁴	97.28	94.13	89.50	81.75	96.06	90.00	85.75	78.75

* "Tr", "Va", "Te1", and "Te2" are the abbreviations of "training accuracy", "validation accuracy", "accuracy on test set with 1.7 m human height", and "accuracy on test set with 1.6 m human height", respectively. The remaining definitions are consistent with Fig. 6. In addition, to ensure the consistency and persuasiveness of the experiments, the image data used before the corner point representation are RTM and DTM, and the image data used after the corner point representation are **R²TM** and **D²TM**.

¹ M1, SIMFNet [56]: The network of the authors' proposed method is equipped with three parallel input branches. However, considering the consistency of the comparison experiments, we remove the link of cadence velocity diagram input, and only use RTM / DTM branches for training.

² M2, DRDSP-PointNet [57]: The method originally has the process of feature dimension reduction, here we refer to the method proposed by the authors that also does the data sparse compression based on OMP. However, the data after corner representation does not perform the sparse compression process.

³ M3, TWR-MDFF [58]: The data format in the feature extraction stage and the FastPCA fusion method both refer to the original paper. The concatenated dimension of "Data Index" is selected to have a dimension of 1024 (256 + 256 + 512).

⁴ M4, TWR-RV-ConvGRU [59]: For the rigor of comparison, the number of nodes in the ConvGRU layer used to extract Range-Time-Doppler data in the proposed method is still set to 60, which is consistent with M1.

groundtruth is all less than 0.3, which implies that the corner point cloud can represent the Doppler and micro-Doppler signature related to human motion [53]. On **R²TM**, the order of PSNRs for two different data sets is: Simulated > Measured. All the PSNRs are higher than 19 dB. On **D²TM**, the order of PSNRs for two different data sets is also: Simulated > Measured. All the PSNRs are higher than 18.5 dB. From the above analysis, the extracted corner feature maps can reflect approximately human motion patterns.

Next, the noise robustness of the proposed micro-Doppler corner representation is verified by manually adding Gaussian noise of different powers to the **R²TM** and **D²TM**. The SNRs of the images are decreased by 4 dB, 8 dB, and 12 dB. The results for earth mover's distance are shown in Fig. 11, which are calculated by arithmetically averaging over 12 different activities. The results show that the distance is not significantly degraded. For relatively noisy environments that the reduction of SNR exceeds 10 dB, the distance is still below 0.5, which is within an acceptable level [53].

C. Validation of Corner Representation Theory: Feature Embedding, Generalization Capability, and Scenario Adaptation

First, T-SNE is employed to analyze the feature separability of different activities in two different scenarios before and after the corner representation. T-SNE visualizes the data by

TABLE VII

COMPARISON OF THE IMPACT ON THE GENERALIZATION CAPABILITY OF BACK-END RECOGNITION MODELS UNDER DIFFERENT WALL SCENARIOS*.

(%)	Sim				Sim Inhomogeneous Wall ¹			
	Tr	Va	Te1	Te2	Tr	Va	Te1	Te2
Methods Before Corner Representation								
M1	95.41	94.00	80.50	75.75	93.25	90.88	86.50	78.00
M2	95.44	92.00	79.50	71.25	93.59	86.38	83.25	73.25
M3	90.84	85.63	74.00	65.50	89.00	88.50	75.50	68.25
M4	98.97	94.13	80.00	72.25	95.47	93.63	85.00	79.25
★ Methods After Corner Representation ★								
M1	93.22	90.63	88.00	82.25	91.16	90.63	87.25	81.00
M2	96.78	93.38	90.50	84.75	94.97	92.38	89.25	84.75
M3	93.91	90.75	86.50	81.00	92.38	88.25	83.50	78.50
M4	97.28	94.13	89.50	81.75	96.47	93.75	88.00	80.50

* All abbreviations and parameter settings are consistent with TABLE VI.

¹ According to the experimental setup, the original dataset is constructed using a homogeneous wall. The dataset used for the comparison, on the other hand, considers an inhomogeneous wall setup consistent with the work [60].

mapping the high-dimensional profiles to the low-dimensional space while maintaining the local similarity relationship between data points [55]. The results are shown in Fig. 12 and 13. From the results, the inter-class feature separation of **R²TM** and **D²TM** obtained from simulated scenario is larger than measured scenario. After corner extraction and representation, the average distance of the intra-class data are all reduced compared to the original profiles while keeping the coordinate scale of the mapping space constant in [0, 1]. Furthermore, compared with the results of the raw **R²TM** and **D²TM**, the corner feature maps show larger inter-class distance and obvious clustering center. More importantly, the outstanding characteristics of corner representation makes potential benefits for high recognition accuracy and generalization capability.

Next, the generalization capability of the proposed micro-Doppler corner representation method is demonstrated by introducing some existed back-end recognition methods. The data sets are divided into training sets, validation sets and test sets. The training sets are used for model training, the validation sets are used for tuning the hyperparameters of the model and for model selection, and the test sets are used to evaluate the performance of the models. Note that, the testers employed in validation sets are the same as those in training sets, while the testers employed in test sets are different. Thus, the difference of the recognition accuracy between the test sets and validation sets reflect the model's generalization ability on different testers. The training and validation sets are generated based on two different testers with 1.8 m in height. The test sets are generated based on two different testers with 1.7 m and 1.6 m in height. The **R²TM** and **D²TM** for each scene are randomly sliced into 3200 training samples, 800 validation samples, and 400 test samples, where activity state S1 accounts for 17.5% of the total data, and S2 ~ S12 each accounts for 7.5% of the total data. The amount of data for different tester identities is the same for all types of activities.

The selected recognition models include four frontier works: (1) M1: SIMFNet, (2) M2: DRDSP-PointNet, (3) M3: TWR-MDFF, and (4) M4: TWR-RV-ConvGRU. In all recognition

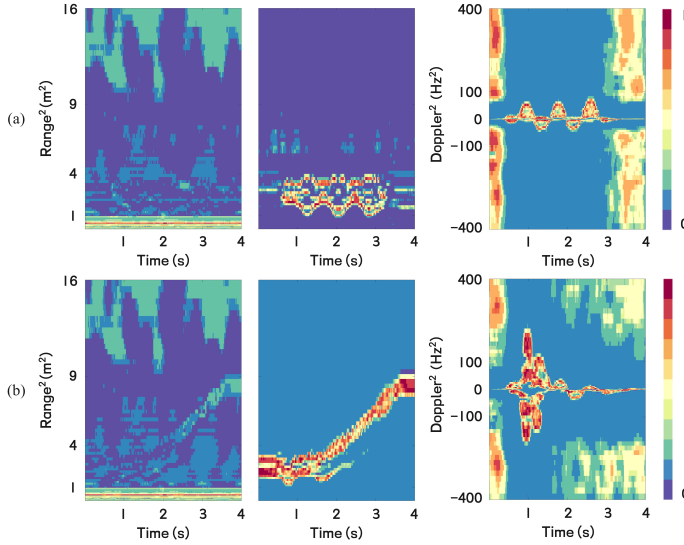


Fig. 14. Simulated R^2TM and D^2TM under inhomogeneous wall [60], [64]: (a) Punching activity, (b) Walking activity as an example. The first row presents the raw simulation in the form of R^2TM . The second row presents the processed R^2TM . The third row presents the processed D^2TM .

models, the training optimizer keeps consistent with each other and Adam is used with the initial learning rate 0.00147. The training process is continued until convergence and the model of the last epoch is used for inference.

The recognition accuracy of different methods is shown in TABLE VI. The training accuracy exceeds 90%, and validation accuracy exceeds 85%, which proves that these methods can achieve convergence in both simulated and measured scenarios, and the inference results are valid. The test accuracy of different recognition models using RTM, DTM as input drops heavily compared with validation accuracy. From the perspective of modeling, SIMFNet, TWR-MDFF, and TWR-RV-ConvGRU that do convolution, multi-scale conversion, multi-link fusion, or attention-based feature extraction on images have certain degree of generalization capability. DRDSP-PointNet that inherently has feature dimension reduction achieves relatively better generalization performance. By comparing the recognition accuracy under different testers, i.e. $Te_1 > Te_2$, it can be concluded that the Doppler and micro-Doppler signature are heavily influenced by the testers' height. All the methods suffers from an accuracy degradation of more than 15% when there is a large difference between height (Va versus Te_2).

After corner representation, the performance of most of these methods on the training, validation, and test sets improves to a certain degree. The accuracy gaps between Va , Te_1 , and Te_2 are reduced, which shows that corner representation can effectively focus on the key information of human motion micro-Doppler signature and improves generalization capability to testers with different height.

The performance of the generalization ability of the proposed method under different complex wall scenarios is also verified. In this case, both homogeneous and inhomogeneous walls and data generation methods refer to the work [60]. The signal model and the parameters of the TWR system

used are kept consistent with the experimental setup described earlier in this paper. Examples of data visualization based on the inhomogeneous wall simulation is shown in Fig. 14 [61]–[64], and the comparisons of the accuracy of different existing recognition methods is shown in TABLE VII. From the results, it can be seen that the presence of a inhomogeneous wall brings amplitude distortion to the micro-Doppler signature of indoor human motion. The amplitude distortion introduced by inhomogeneous wall with respect to homogeneous wall is reduced to almost zero only after the clutter and noise suppression, and the normalization are performed. However, the curvature and Doppler frequency of the trace corresponding to each human limb nodes do not change. Thus the positions of the corner features analyzed from the kinematic model should not change. Comparing the validation and testing accuracy of the existing methods before and after the corner representation, it can be seen that the proposed method remains good generalization ability even in the presence of inhomogeneous wall.

D. Discussions

The effectiveness and generalization ability of the proposed method are proved both mathematically and experimentally. However, there are still some limitations and potentials, which are worth investing in further research, including:

1. Limitations on Model Complexity: Although the lowest feature dimension constraints and simplicity that can be computed through the proposed Boulic-sinusoidal pendulum kinematic model, it is still flawed for portraying the complex stochasticity of real human motion. Modeling studies that trade-off between simplicity and realism are still necessary.

2. Potentials on the Method of Calculating the Optimal Corner Points: The paper proposes a method using the summation of the order information of the nodal curves in the kinematic model. The method shows theoretical soundness and can be analyzed in depth for their respective practical value in further researches.

V. CONCLUSION

In this paper, we have proposed a corner-based micro-Doppler signature representation method to address the issue of accuracy loss for various testers. This paper has provided the joint Boulic-sinusoidal pendulum model to characterize indoor human activities as well as a refined signal model of TWR echoes. Additionally, the paper has analyzed the micro-Doppler corner feature for human motion on R^2TM and D^2TM , and computed the minimum number of corner points needed to describe the Doppler and micro-Doppler information. Furthermore, we have given a feasible corner extraction method based on SOGGDD filter. Both simulated and measured experiments are conducted to verify the proposed theory. The findings have shown that the suggested micro-Doppler corners could accurately represent the motion characteristics of human limb nodes, which shows great benefits for high recognition accuracy and generalization capability. Our future work will focus on proposing a more accurate and intelligent micro-Doppler corner detection and activity recognition method.

REFERENCES

- [1] B. Erol and M. G. Amin, "Radar Data Cube Processing for Human Activity Recognition Using Multisubspace Learning," *IEEE Trans. Aerosp. Electron. Syst.*, vol. 55, no. 6, pp. 3617–3628, Dec. 2019.
- [2] Y. Yao, W. Liu, G. Zhang, and W. Hu, "Radar-Based Human Activity Recognition Using Hyperdimensional Computing," *IEEE Trans. Microw. Theory and Tech.*, vol. 70, no. 3, pp. 1605–1619, Mar. 2022.
- [3] F. Qi, Z. Li, Y. Ma, F. Liang, H. Lv, J. Wang, and A. E. Fathy, "Generalization of Channel Micro-Doppler Capacity Evaluation for Improved Finer-Grained Human Activity Classification Using MIMO UWB Radar," *IEEE Trans. Microw. Theory and Tech.*, vol. 69, no. 11, pp. 4748–4761, Nov. 2021.
- [4] S. Subedi, Y. D. Zhang, M. G. Amin, and B. Himed, "Group Sparsity Based Multi-Target Tracking in Passive Multi-Static Radar Systems Using Doppler-Only Measurements," *IEEE Trans. Signal Process.*, vol. 64, no. 14, pp. 3619–3634, Jul. 2016.
- [5] X. Qiao, M. G. Amin, T. Shan, Z. Zeng, and R. Tao, "Human Activity Classification Based on Micro-Doppler Signatures Separation," *IEEE Trans. Geosci. Remote Sens.*, vol. 60, pp. 1–14, 2022.
- [6] V. C. Chen, Fayin Li, Shen-Shyang Ho, and H. Wechsler, "Micro-doppler effect in radar: phenomenon, model, and simulation study," *IEEE Trans. Aerosp. Electron. Syst.*, vol. 42, no. 1, pp. 2–21, Jan. 2006.
- [7] S. Zhu, R. G. Guendel, A. Yarovoy, and F. Fioranelli, "Continuous Human Activity Recognition With Distributed Radar Sensor Networks and CNN-RNN Architectures," *IEEE Trans. Geosci. Remote Sens.*, vol. 60, pp. 1–15, 2022.
- [8] J. He, Z. Ren, W. Zhang, Y. Jia, S. Guo, and G. Cui, "Fall Detection Based on Parallel 2DCNN-CBAM With Radar Multidomain Representations," *IEEE Sens. J.*, vol. 23, no. 6, pp. 6085–6098, Mar. 2023.
- [9] H. Du, T. Jin, Y. Song, Y. Dai, and M. Li, "A Three-Dimensional Deep Learning Framework for Human Behavior Analysis Using Range-Doppler Time Points," *IEEE Geosci. Remote Sens. Lett.*, vol. 17, no. 4, pp. 611–615, Apr. 2020.
- [10] J. Zhu, Y. Song, N. Jiang, Z. Xie, C. Fan, and X. Huang, "Enhanced Doppler Resolution and Sidelobe Suppression Performance for Golay Complementary Waveforms," *Remote Sens.*, vol. 15, no. 9, p. 2452, May 2023.
- [11] Fugui Qi, Zhao Li, Fulai Liang, Hao Lv, Qiang An, and Jianqi Wang, "A novel time-frequency analysis method based on HHT for finer-grained human activity using SFCW radar," in *Proc. Prog. Electromagn. Res. Symp.*, Aug. 2016.
- [12] Z. Zheng, J. Pan, Z. Ni, C. Shi, S. Ye, and G. Fang, "Human Posture Reconstruction for Through-the-Wall Radar Imaging Using Convolutional Neural Networks," *IEEE Geosci. Remote Sens. Lett.*, vol. 19, pp. 1–5, 2022.
- [13] B. Li, Y. Yang, L. Yang, and C. Fan, "Objective Evaluation of Clutter Suppression for Micro-Doppler Spectrograms of Hand Gesture/Sign Language Based on Pseudo-Reference Image," *IEEE Trans. Geosci. Remote Sens.*, vol. 61, pp. 1–13, 2023.
- [14] M. Ding, Y. Ding, Y. Peng, and J. Cao, "CNN-Based Time-Frequency Image Enhancement Algorithm for Target Tracking Using Doppler Through-Wall Radar," *IEEE Trans. Geosci. Remote Sens.*, vol. 20, pp. 1–5, 2023.
- [15] J. Chen, S. Guo, H. Luo, N. Li, and G. Cui, "Non-Line-of-Sight Multi-Target Localization Algorithm for Driver-Assistance Radar System," *IEEE Trans. Veh. Technol.*, vol. 72, no. 4, pp. 5332–5337, Apr. 2023.
- [16] Y. Xiang, S. Guo, S. Xia, X. Gu, J. Chen, and G. Cui, "NLOS Target Positioning Method Based on UAV Millimeter-Wave Radar," *IEEE Sens. J.*, vol. 24, no. 2, pp. 1975–1987, Jan. 2024.
- [17] A. Alkasimi, A.-V. Pham, C. Gardner, and B. Funsten, "Human Activity Recognition Based on 4-Domain Radar Deep Transfer Learning," in *Proc. IEEE Radar Conf.*, May 2023.
- [18] Z. Zhang, P. O. Pouliquen, A. Waxman, and A. G. Andreou, "Acoustic micro-Doppler radar for human gait imaging," *J. Acoust. Soc. Am.*, vol. 121, no. 3, pp. EL110–EL113, Feb. 2007.
- [19] H. Gao, L. Xie, S. Wen, and Y. Kuang, "Micro-Doppler Signature Extraction from Ballistic Target with Micro-Motions," *IEEE Trans. Aerosp. Electron. Syst.*, vol. 46, no. 4, pp. 1969–1982, Oct. 2010.
- [20] G. E. Smith, K. Woodbridge, and C. J. Baker, "Radar Micro-Doppler Signature Classification using Dynamic Time Warping," *IEEE Trans. Aerosp. Electron. Syst.*, vol. 46, no. 3, pp. 1078–1096, Jul. 2010.
- [21] F. Fioranelli, M. Ritchie, H. Griffiths, and H. Borrión, "Classification of loaded/unloaded micro-drones using multistatic radar," *Electron. Lett.*, vol. 51, no. 22, pp. 1813–1815, Oct. 2015.
- [22] L. Du, L. Li, B. Wang, and J. Xiao, "Micro-Doppler Feature Extraction Based on Time-Frequency Spectrogram for Ground Moving Targets Classification With Low-Resolution Radar," *IEEE Sens. J.*, vol. 16, no. 10, pp. 3756–3763, May 2016.
- [23] V. C. Chen, D. Tahmouh, and W. J. Miceli, Eds., *Radar Micro-Doppler Signatures: Processing and Applications*, vol. 34. 2014.
- [24] Z. Zeng, M. G. Amin, and T. Shan, "Automatic Arm Motion Recognition Based on Radar Micro-Doppler Signature Envelopes," *IEEE Sens. J.*, vol. 20, no. 22, pp. 13523–13532, Nov. 2020.
- [25] F. Fioranelli, M. Ritchie, and H. Griffiths, "Classification of Unarmed/Armed Personnel Using the NetRAD Multistatic Radar for Micro-Doppler and Singular Value Decomposition Features," *IEEE Geosci. Remote Sens. Lett.*, vol. 12, no. 9, pp. 1933–1937, Sep. 2015.
- [26] X. Li, Y. He, and X. Jing, "A Survey of Deep Learning-Based Human Activity Recognition in Radar," *Remote Sens.*, vol. 11, no. 9, p. 1068, May 2019.
- [27] A. D. Singh, S. S. Sandha, L. Garcia, and M. Srivastava, "RadHAR: Human Activity Recognition from Point Clouds Generated through a Millimeter-wave Radar" in *Proc. ACM Works. Millim. Wave Netw. Sens. Syst.*, Oct. 2019.
- [28] C. Cheng, F. Ling, S. Guo, G. Cui, Q. Jian, C. Jia, and Q. Ran, "A Real-time Human Activity Recognition Method for Through-the-Wall Radar," in *Proc. IEEE Radar Conf.*, Sep. 2020.
- [29] F. Ahmad, M. G. Amin and G. Mandapati, "Autofocusing of through-the-wall radar imagery under unknown wall characteristics," *IEEE Trans. Image Process.*, vol. 16, no. 7, pp. 1785–1795, July 2007.
- [30] Y. Jia et al., "ResNet-based counting algorithm for moving targets in through-the-wall radar," *IEEE Geosci. Remote Sens. Lett.*, vol. 18, no. 6, pp. 1034–1038, June 2021.
- [31] X. Yang, P. Chen, M. Wang, S. Guo, C. Jia and G. Cui, "Human Motion Serialization Recognition With Through-the-Wall Radar," *IEEE Access*, vol. 8, pp. 186879–186889, 2020.
- [32] S. Guo et al., "Graph Matching Based Image Registration for Multi-View Through-the-Wall Imaging Radar," *IEEE Sens. J.*, vol. 22, no. 2, pp. 1486–1494, 15 Jan. 15, 2022.
- [33] W. Gao, X. Yang, X. Qu and T. Lan, "TWR-MCAE: A Data Augmentation Method for Through-the-Wall Radar Human Motion Recognition," *IEEE Trans. Geosci. Remote Sens.*, vol. 60, pp. 1–17, 2022, Art no. 5118617.
- [34] X. Qu, W. Gao, H. Meng, Y. Zhao and X. Yang, "Indoor Human Behavior Recognition Method Based on Wavelet Scattering Network and Conditional Random Field Model," *IEEE Trans. Geosci. Remote Sens.*, vol. 61, pp. 1–15, 2023, Art no. 5104815.
- [35] X. Yang, W. Gao, X. Qu, P. Yin, H. Meng and A. E. Fathy, "A Lightweight Multiscale Neural Network for Indoor Human Activity Recognition Based on Macro and Micro-Doppler Features," *IEEE Intern. Things J.*, vol. 10, no. 24, pp. 21836–21854, 15 Dec. 15, 2023.
- [36] N. Rojhani, M. Passafiume, M. Sadeghibakhii, G. Collodi, and A. Cidronali, "Model-Based Data Augmentation Applied to Deep Learning Networks for Classification of Micro-Doppler Signatures Using FMCW Radar," *IEEE Trans. Microw. Theory Tech.*, vol. 71, no. 5, pp. 2222–2236, May 2023.
- [37] M. S. Seyfioglu and S. Z. Gurbuz, "Deep Neural Network Initialization Methods for Micro-Doppler Classification With Low Training Sample Support," *IEEE Geosci. Remote Sens. Lett.*, vol. 14, no. 12, pp. 2462–2466, Dec. 2017.
- [38] P. Thanapol, K. Lavangnananda, P. Bouvry, F. Pinel, and F. Leprevost, "Reducing Overfitting and Improving Generalization in Training Convolutional Neural Network (CNN) under Limited Sample Sizes in Image Recognition," in *Proc. Intern. Conf. Inform. Technol.*, Oct. 2020.
- [39] T. Isomura and T. Toyozumi, "Dimensionality reduction to maximize prediction generalization capability," *Nat. Mach. Intell.*, vol. 3, no. 5, pp. 434–446, Apr. 2021.
- [40] S. Sundar Ram and H. Ling, "Simulation of human microDopplers using computer animation data," in *Proc. IEEE Radar Conf.*, Rome, Italy, 2008, pp. 1–6.
- [41] E. Arbabi, R. Boulic, and D. Thalmann, "A Fast Method for Finding Range of Motion in the Human Joints," in *Proc. Annu. Intern. Conf. IEEE Engin. Medic. Biol. Society*, Aug. 2007.
- [42] R. Zhang, Z. Zhang, X. Zhang, Y. Tang, and W. Sheng, "Phase compensation transform for human detection with LFM CW radar," *Signal Process.*, vol. 172, p. 107565, Jul. 2020.
- [43] W. Guo, S. Qiu, P. Wang, W. Sheng, and J. Deng, "Foot placement analysis of human walking based on capture point of linear inverted pendulum model," in *Proc. Intern. Conf. Inform. Autom.*, Jul. 2017.

- [44] Y. Wang, L. Zhang, S. Wang, T. Zhao, Y. Wang, and Y. Li, "Radar HRRP target recognition using scattering centers fuzzy matching," in *Proc. CIE Intern. Conf. Radar*, Oct. 2016.
- [45] Y. Lei, U. Dogan, D.-X. Zhou, and M. Kloft, "Data-Dependent Generalization Bounds for Multi-Class Classification," *IEEE Trans. Inform. Theory*, vol. 65, no. 5, pp. 2995–3021, May 2019.
- [46] X. Shen and L. Wang, "Generalization error for multi-class margin classification," *Electron. J. Stat.*, vol. 1, no. none, Jan. 2007.
- [47] P. L. Bartlett and S. Mendelson, "Rademacher and Gaussian complexities: Risk bounds and structural results," *J. Mach. Learn. Res.*, vol. 3, pp. 463–482, Mar. 2003.
- [48] B. Zhu, L. Tang, X. Wang, and X. Cai, "A pragmatic scheme of SNR estimation for optical remote sensing images," in *Proc. IEEE Intern. Conf. Comput. Sci. Autom. Engin.*, May 2012.
- [49] S. Vishwakarma, W. Li, C. Tang, K. Woodbridge, R. Adve, and K. Chetty, "SimHumalator: An Open-Source End-to-End Radar Simulator for Human Activity Recognition," *IEEE Aeros. Electron. Syst. Mag.*, vol. 37, no. 3, pp. 6–22, Mar. 2022.
- [50] S. Z. Gurbuz, M. M. Rahman, E. Kurtoglu, T. Macks, and F. Fioranelli, "Cross-frequency training with adversarial learning for radar micro-Doppler signature classification (Rising Researcher)," *Radar Sens. Technol.* XXIV, May 2020.
- [51] W. Zhang and C. Sun, "Corner Detection Using Second-Order Generalized Gaussian Directional Derivative Representations," *IEEE Trans. Pattern Anal. Mach. Intell.*, vol. 43, no. 4, pp. 1213–1224, Apr. 2021.
- [52] E. Levina and P. Bickel, "The Earth Mover's distance is the Mallows distance: some insights from statistics," in *Proc. IEEE Intern. Conf. Comput. Vis.*, 2001.
- [53] W. Yuan, T. Khot, D. Held, C. Mertz and M. Hebert, "PCN: Point Completion Network," in *Proc. Intern. Conf. 3D Vision*, Verona, Italy, 2018, pp. 728–737.
- [54] A. Hore and D. Ziou, "Image Quality Metrics: PSNR vs. SSIM," in *Proc. Intern. Conf. Patt. Recog.*, Aug. 2010.
- [55] J. Geng, H. Wang, J. Fan, and X. Ma, "SAR Image Classification via Deep Recurrent Encoding Neural Networks," *IEEE Trans. Geosci. Remote Sens.*, vol. 56, no. 4, pp. 2255–2269, Apr. 2018.
- [56] X. Yu, Z. Cao, Z. Wu, C. Song, and Z. Xu, "Sample Inter-correlation-Based Multidomain Fusion Network for Aquatic Human Activity Recognition Using Millimeter-Wave Radar," *IEEE Geosci. Remote Sens. Lett.*, vol. 20, pp. 1–5, 2023.
- [57] C. Ding, L. Zhang, H. Chen, H. Hong, X. Zhu, and F. Fioranelli, "Sparsity-Based Human Activity Recognition With PointNet Using a Portable FMCW Radar," *IEEE Intern. Things J.*, vol. 10, no. 11, pp. 10024–10037, Jun. 2023.
- [58] H. Xu, Y. Li, Y. Li, J. Li, B. Wang, and L. Liu, "Through-Wall Human Motion Recognition Using Random Code Radar Sensor With Multi-Domain Feature Fusion," *IEEE Sens. J.*, vol. 22, no. 15, pp. 15123–15132, Aug. 2022.
- [59] L. Tang, S. Guo, Q. Jian, G. Cui, L. Kong, and X. Yang, "Through-Wall Human Activity Recognition With Complex-Valued Range-Time-Doppler Feature and Region-Vectorization ConvGRU," *IEEE Trans. Geosci. Remote Sens.*, vol. 61, pp. 1–14, 2023.
- [60] S. S. Ram, C. Christianson, Y. Kim and H. Ling, "Simulation and Analysis of Human Micro-Dopplers in Through-Wall Environments," *IEEE Trans. Geosci. Remote Sens.*, vol. 48, no. 4, pp. 2015–2023, April 2010.
- [61] K. Yasmeen and S. S. Ram, "Estimation of Electrical Characteristics of Inhomogeneous Walls Using Generative Adversarial Networks," *IEEE J. Sel. Top. Appl. Earth Obs. Remote Sens.*, vol. 16, pp. 7009–7023, 2023.
- [62] S. Maiti and A. Bhattacharya, "Microwave Detection of Respiration Rate of a Living Human Hidden Behind an Inhomogeneous Optically Opaque Medium," *IEEE Sens. J.*, vol. 21, no. 5, pp. 6133–6144, 1 March 2021.
- [63] M. Dogan and G. Turhan-Sayan, "Through-the-wall target detection using gpr A-Scan data: Effects of different wall structures on detection performance," in *Proc. Intern. Electrom. Compat. Conf.*, Ankara, Turkey, 2017, pp. 1–5.
- [64] C. Warren, A. Giannopoulos, and I. Giannakis, "gprMax: Open source software to simulate electromagnetic wave propagation for Ground Penetrating Radar," *Comput. Physics Commun.*, vol. 209, pp. 163–170, Dec. 2016.



His current research interests include the phase array radar, ground-penetrating radar and through-the-wall radar.



Weicheng Gao Weicheng Gao (Graduate Student Member, IEEE), received his B.S. degree in Beijing Institute of Technology in 2022. He is pursuing the Ph.D. degree at the Research Lab of Radar Technology, BIT. He is selected as a member of the China Association for Science and Technology (CAST) Talent Program.

His research interests are mainly focused on mathematical theory of radar signal processing and through-the-wall radar human activity recognition.



Xiaodong Qu Xiaodong Qu (Member, IEEE), associate researcher, received the B.S. degree from Xidian University, Xi'an, China, in 2012, and the Ph.D. degree from the University of Chinese Academy of Sciences, Beijing, China, in 2017.

His research interests mainly include array signal processing, through-the-wall radar imaging.



Zeyu Ma Zeyu Ma (Student Member, IEEE), received the B.S. degree in automation from North China Electric Power University, Beijing, China, in 2022. He is currently pursuing the M.S. degree in the School of Information and Electronics at the Beijing Institute of Technology.

His research interests include through-the-wall radar moving targets location and tracking.



Hao Zhang Hao Zhang (Student Member, IEEE), was born in Shanxi Province, China, in 2000. He received the B.S. degree from the North China Electric Power University, Baoding, China, in 2022. He is currently working toward the M.S. degree at the School of Information and Electronics, Beijing Institute of Technology (BIT), Beijing, China.

His current research interests are in the areas of moving target localization with unmanned aerial vehicle based through-the-wall radar.